5-1-2016

Experimental Verification of the Concept of the Relativistic Magnetron with Simple Mode Converter

Jeremy McConaha

Follow this and additional works at: https://digitalrepository.unm.edu/ece_etds

Jeremy McConaha
_____
Candidate

Electrical and Computer Engineering
_____
Department

This thesis is approved, and it is acceptable in quality and form for publication:

Approved by the Thesis Committee:

Dr. Edl Schamiloglu , Chairperson
_____

Dr. Sarita Prasad
_____

Dr. Mark Gilmore
_____

_
_____

_____

_____

_____

_____

i

Experimental Verification of the Concept of the Relativistic Magnetron with Simple Mode Converter

By

Jeremy McConaha

B.S., Electrical Engineering, University of New Mexico, 2014

THESIS

Submitted in Partial Fulfillment of the Requirements for the Degree of

Masters of Science Electrical Engineering

The University of New Mexico
Albuquerque, New Mexico

May, 2016

DEDICATIONS

I would like to dedicate this thesis to everyone who has believed in me, and given me the chance to prove myself.

ACKNOWLEDGMENTS

Experimental Verification of the Concept of the Relativistic Magnetron with Simple Mode Converter

By Jeremy McConaha

B.S., Electrical Engineering, University of New Mexico, 2014

M.S., Electrical Engineering, University of New Mexico, 2016

Abstract

A compact A6 relativistic magnetron with a simple mode converter for axial TE_{11}-mode extraction was recently designed at the University of New Mexico. With the standard A6 magnetron operating in the π-mode it is possible to implement a simple mode converter to radiate a TE_{11}-mode axially through a cylindrical waveguide whose radius is the same as the anode cavity radius. The proposed mode converter implements an anode end cap that electrically opens diametrically opposite cavities that produce an electric field polarization corresponding to that of the of the TE_{11}-mode in a cylindrical waveguide. The TE_{11}-mode has a Gaussian-like profile with maximum electric field on axis, and is desirable for applications.

In this work an extensive parametric sweep was conducted using the three dimensional particle-in-cell (PIC) code MAGIC to optimize the mode converter design. The cathode used is the transparent cathode with a radius chosen to favor π-mode operation of the magnetron.

The trends observed in simulation have been verified experimentally. Simulations showed magnetron operation in π-mode at 2.33 GHz, and the output waveguide mode for these operating conditions was verified to be the TE_{11}-mode. In experiments performed at approximately the same operating magnetic field a single frequency RF signal at 2.33 GHz was detected. A neon grid used for mode detection confirmed a maximum in the center, which is indicative of the TE_{11}-mode. The radiated power is in the order of ~100's of MW.

Table of Contents

List of Figures

Chapter 1

Introduction

The objective of this study is to demonstrate the viability of a novel type of mode converter for the standard A6 magnetron. This chapter details the history of magnetrons, and the applications of high power microwaves. Several extraction designs are discussed.

1.1.1 Magnetron History

The first magnetron was invented in 1912 by Arthur W. Hull of General Electric Research Laboratory while searching for an alternative to the vacuum-tube diode [1]. However, this magnetron had a smooth bore anode block, which exhibited very low output power and poor efficiency. In 1924, Czechoslovakian scientist August Zacek and German scientist Erich Habann produced oscillations of 100 MHz to 1 GHz using a cylindrical split anode magnetron [1]. This discovery led to the search for a more reliable and higher power source in the 10 cm wavelength region [2]. The motivation for finding this short-wavelength source was early research into radar systems for the impending global crisis which came to be called the Second World War [1]. During this period, the radar systems primarily used the frequency stable but low power klystrons designed by the Varian brothers in 1937 [3].

In 1940, Harry Boot and John Randall realized that in order to generate higher output powers, higher current electron beams were needed. At the time it was not possible to increase the current of the beams in klystrons, but it was possible to incorporate high input powers with the coaxial magnetron designs. This led to the combination of the slow wave (cavity) structures of klystrons with magnetron designs [2]. This discovery led to the development of a cavity magnetron operating in the 10 cm wavelength range with a microwave output power of roughly 10 kW, compared to the 10's W produced by klystrons. Although the early magnetrons were not very frequency stable, Boot and Randall were able to build radar systems capable of detecting a submarine periscope at a range of 7 miles by September 1940. It is now widely believed that the advancements in radar made by the Allies during the war had a greater effect on its outcome than the advent of the atomic bomb [1].

With advancements in modern pulsed power techniques in the late 1960's, cavity magnetrons and many other microwave devices were further explored with the added capabilities of much higher operating voltages, in the 100's of kV range, and currents in the 1-10's kA range. One such development was the 6-cavity (A6) magnetron in the relativistic regime introduced by Palevsky and Bekefi at MIT in 1979 (1976), which had microwave power levels exceeding 900 MW in the S-band with an applied voltage of 400 kV. This magnetron has become the most widely studied device for the generation of high power microwaves [4].

1.1.2 Applications of HPM

The applications of high power microwave (HPM) systems range from short pulse radars to directed energy weapons designed for the suppression of or interference with radio-electronic devices [5]. The latter are designed to cause physical damage or temporary disruption to electronic systems. Additionally, HPM systems are used for jamming RF radar receivers, as well as spoofing the radar systems. Another recently developed less-than-lethal weapon is the active denial systems (ADS), designed for riot control and mob dispersion. It works by transmitting a high frequency, highly directed beam that is absorbed by the outer layer of the individual's skin, causing an intense burning sensation. Some additional applications of HPM systems are the heating of plasma for fusion devices, powering accelerator cavities, power beaming, and the excitation of gas lasers, among others [5].

Although there are many applications of HPM systems, the most researched application is directed energy weapons. Examples are E-bombs [5] and CHAMP, which is an HPM system built into a cruise missile. CHAMP was a joint venture led by Boeing and the Air Force Research Laboratory, that was successfully tested in 2012.

It is very important when designing a HPM system to consider the efficiency of the system and the source, the output power of the source, and the size of the system. The A6 relativistic magnetron is an ideal candidate for use in HPM systems due to its high efficiency and its GW class power production capability.

1.2.1 Summary of Axial Extraction Designs

The A6 magnetron, like most relativistic magnetrons, utilizes a radial extraction scheme for radiating the microwaves generated in the interactions of the magnetron. Radial extraction is accomplished by radiating the power through a slot located in one or more of the cavities.

Conversely, axial extraction employs a scheme to radiate the power through the axial end of the cavities (slow-wave structure). This allows the operating mode of the magnetron (π or 2π-mode) to excite a mode of interest in the output waveguide of the magnetron. Axial extraction in a relativistic magnetron was first tested in Russia in the late 1970's [19]. This scheme is known as the magnetron with diffraction output (MDO), and is accomplished by adding deep flaring cavities in a conical horn antenna. However, the initial attempt at demonstrating this design reported very low efficiencies. This was due to the output waveguide aperture being below cutoff and the shallow cavity flare [6]. In 2007, the MDO was revisited by Daimon and Jiang at the Nagaoka University of Technology in Japan. They presented improvements to the efficiency up to 37% [7], which were also experimentally demonstrated [8]. This led to further investigation of the MDO at the University of New Mexico (UNM), where efficiencies of ~70% and output powers above 1 GW in a TE_{31}-mode were presented and experimentally verified [9],[10]. This was accomplished by optimizing the cavity and vane flare, and implementing the transparent cathode [11]. The optimized MDO design is shown in Fig. 1.1.
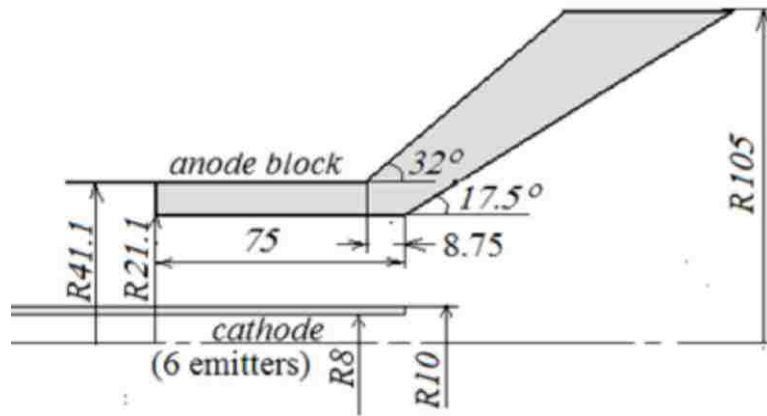
Figure 1.1 The ideal dimensions of the 70% efficient MDO from UNM [6].

Additionally, the MDO can be modified to output a TE_{11}-mode, at a reduced power and efficiency. However, the MDO is a very large package, requiring a beam dump with a sufficient length to capture the leakage electrons.

The second design, which was presented by the Chinese National University of Defense Technology, is similar to the early MDO designs in that the magnetron vanes are continued into the output waveguide by means of a gradual taper. However, the main difference is that the

3

radius of the output waveguide is the same as that of the magnetron, which allows for a much more compact source design. When the magnetron is operating in the π-mode, this design allows a TE_{11}-mode to be excited in the output waveguide. The simulations for this show efficiencies as high as 42% [12]. This design is shown in Fig. 1.2.
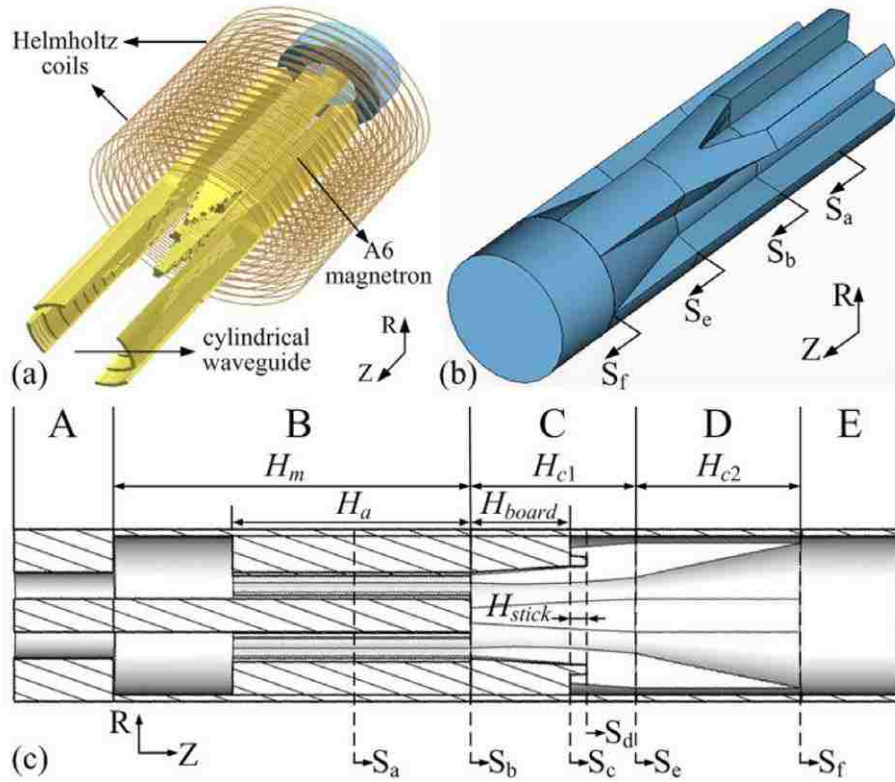
Figure 1.2 The design of the Chinese tapered TE_{11}-mode converter, (A) is a 3D view of the setup, (B) shows the negative of the interior of the magnetron, and (C) is a side view showing the different features in more detail [12].

However, this design presents the issue of complex geometries which are not sufficiently presented and could not be reproduced. Additionally, these simulations were performed using CST's PIC code, and there is some debate as to whether this code provides accurate results when dealing with complex particle motion.

The third design, presented by the same Chinese group, is a compact TE_{10}-mode converter [13]. This design employs a similar vane extension; however, the output aperture is

4

converted axially to a rectangular waveguide with dimensions L=82.2 mm and W=20 mm. This design is shown in Fig. 1.3.
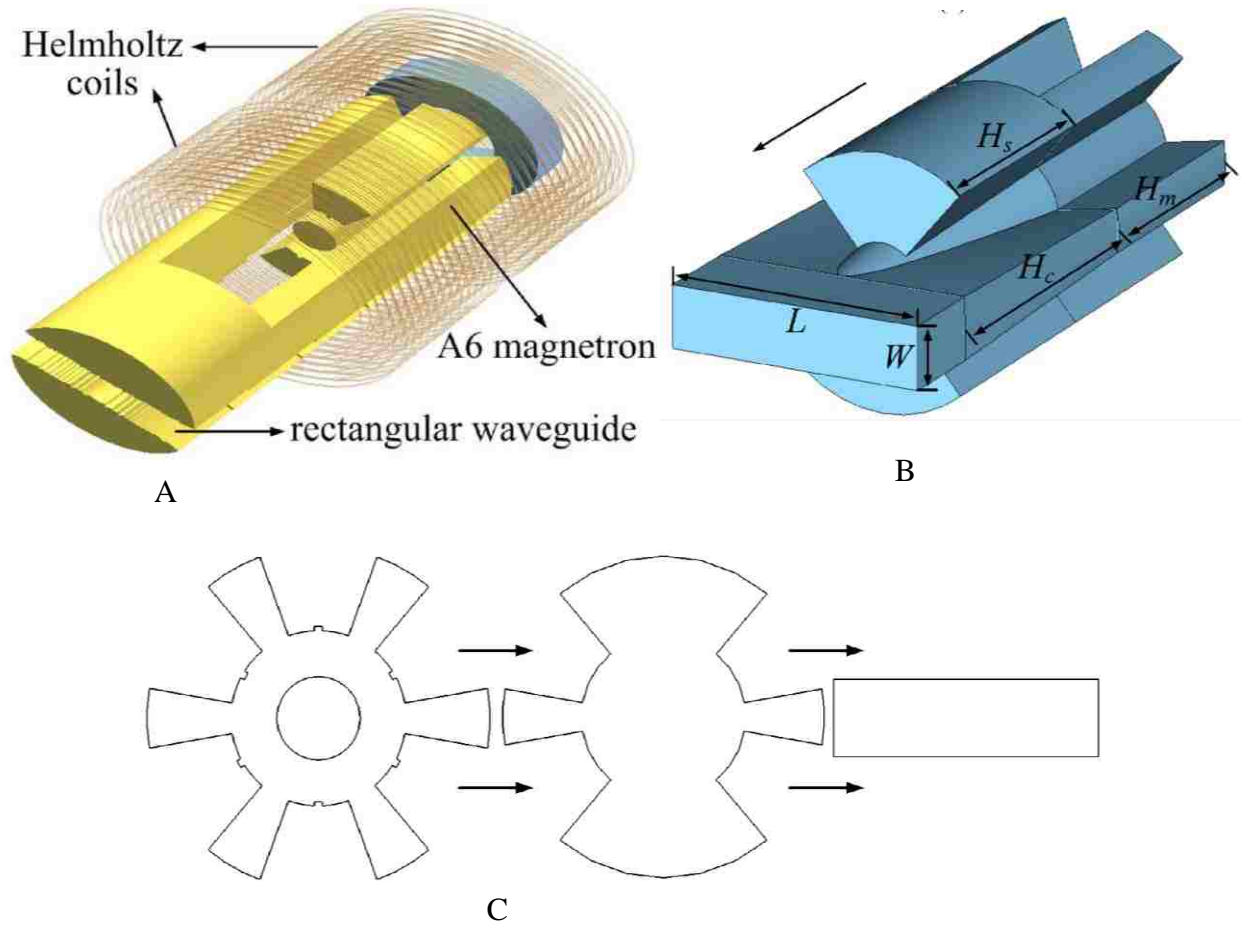
Figure 1.3 The overall design of the TE$_{10}$-mode converter is displayed in A. B shows the negative of the interior of the magnetron, and C shows the conversion of the 6-cavity magnetron to the diametrically opposite cavities, and finally to the rectangular waveguide section [13].

The reported efficiency of design three is 25.3% with an output power of 436 MW and a frequency of 2.52 GHz. The use of a rectangular output aperture is an interesting concept, but this design could not be recreated due to limited information in the paper.

The fourth design is the simple mode converter. This consists of thin metal end caps attached directly to the downstream vanes of the A6 magnetron [14]. This allows for a standard radial extraction magnetron to be converted to an axial extraction scheme. This design will be discussed in further detail in the next section.

1.2.2 The Simple Mode Converter

The simple mode converter implements a cavity end cap with openings which allow the RF to propagate into the circular waveguide. Figure 1.4 is a photograph of the simple mode converter installed on the A6 magnetron. These cavity openings in the end cap are designed such that they electrically open diametrically opposite cavities which exhibit an instantaneous electric field corresponding to that of the TE_{11}-mode [14]. This is possible since for a magnetron operating in the π-mode the electric field distribution in adjacent cavities is 180° out of phase. This ensures that the RF that is allowed to propagate into the cylindrical waveguide has the proper electric field distribution. Additionally, this design implements the transparent cathode designed at UNM [11], [14]. For a 6 cavity magnetron such as the A6, this leads to two extraction schemas; where two diametrically opposite cavities are opened, and where four cavities are opened. This design can be implemented on any magnetron with an even number of cavities, such as 10 and 14 cavity setups [15]. These mode converter configurations are shown in Fig.1.5.

Figure 1.4 The view from the extraction port of the A6 magnetron, with the simple mode converter installed.
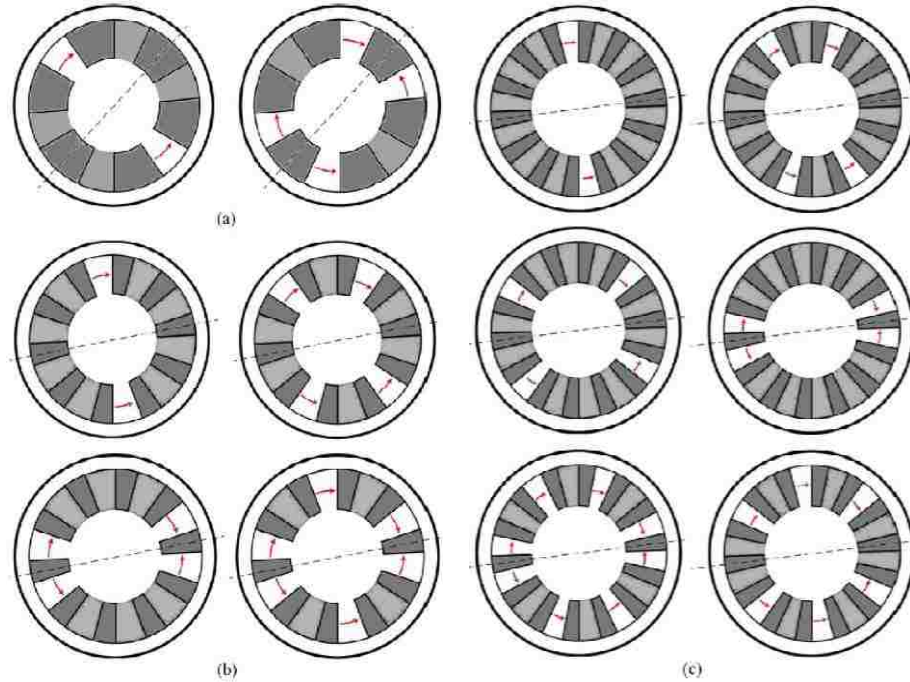
Figure 1.5 The mode converter configuration for (a) a 6-cavity magnetron yields two possible solutions, (b) a 10-cavity magnetron yields four possible solutions, (c) a 14-cavity magnetron yields 6 possible solutions [15]**.**

Additionally, as the output waveguide has the same radius as the magnetron cavities, the electromagnet circuit can be replaced with a high strength neodymium permanent magnet. This addition would greatly reduce the footprint of the HPM system [16], [17]. The rapidly diverging magnetic fields provided by the permanent magnet negate the need for a beam dump, as the leakage electrons will be deposited on the walls of the magnetron, thereby protecting the dielectric output window from damage.

The organization of this thesis is as follows; Chapter 2 discusses the theory of magnetron operation, and design of the simple mode converter. Chapter 3 presents the simulation setup, and optimization of the compact A6 magnetron with simple mode converter. Chapter 4 details the experimental setup used for the verification of the simple mode converter. Finally, Chapter 5 presents the experimental results and conclusion of this thesis.

Chapter 2

Theory of Magnetron Operation, and Concept of Simple Mode Converter

This chapter discusses the basic theory of the magnetron operation, as well as the concept of the simple mode converter.

2.1.1 Physics of Magnetron Operation

Cross-field devices such as magnetrons generate microwaves by converting the potential energy of an electron cloud between the anode and cathode into RF energy. The most common type of magnetron is the cavity magnetron, where a resonant circuit consisting of a number of closely coupled cavities is contained within the anode of the magnetron. The term cross-field device arises from the orthogonal nature of the of the electric and magnetic fields vectors. In the case of a coaxial magnetron, such as MIT's A6 [5], this means that the applied electric field creates a field vector in the radial direction and the magnetic field is applied along the axis of the device.

The surface of the cathode has microprotrusions. When a high voltage is applied across the anode cathode (A-K) gap, the electric field lines concentrate at the tips of these microprotrusions, causing them to ionize and creating a layer of plasma around the cathode. The electrons from this plasma accelerate towards the anode under the influence of the radial electric field [5]. However, the orthogonal magnetic field causes the electrons to undergo an E x B drift about the guiding center. For the cylindrical geometry of a magnetron, this drift v_θ is in the azimuthal direction,

$$v_\theta = \frac{E_r}{B_z} \hspace{4cm} \text{Equation 2.1}$$

where E_r is the applied radial electric field and B_z is the applied axial magnetic field [5].

Although the physics of magnetron operation is complicated, especially in the relativistic regime, it can be described by two guiding equations: the Hull cutoff and the Buneman-Hartree (B-H) conditions. The Hull cutoff condition gives the minimum magnetic field that prevents an electron from reaching the anode, whereas the B-H condition is a synchronous condition related to a specific mode that gives the maximum magnetic field that will result in stable oscillations. These conditions are described in detail in the following section.

2.1.2 Hull Cut-Off Condition and Buneman-Hartree Synchronous Condition

The slow wave structure of a cavity magnetron must be tuned to produce modes with a phase velocity that matches the electron drift velocity produced by the E x B fields. This leads to the first condition of magnetron operation. If the magnetic field is not sufficiently strong the electrons will not undergo a sufficient radial bend back towards the cathode and will, instead, bombard the anode, resulting in the shorting of the magnetron. The minimum magnetic field for a fixed voltage that will sufficiently alter the trajectory of the electrons is given by the Hull cut-off condition,

$$B_c = \frac{mc}{|e|d^*}\sqrt{\frac{2|e|V}{mc^2} + \left(\frac{|e|V}{mc^2}\right)^2} \qquad\qquad \text{Equation 2.2.1}$$

where B_c is the critical magnetic field, m is the mass of an electron, $|e|$ is the electron charge, V is the applied voltage across the A-K gap, c is the speed of light, and d^* is a geometric factor given by

$$d^* = \frac{r_a{}^2 - r_c{}^2}{2r_a} \qquad\qquad \text{Equation 2.2.2}$$

where r_a is the anode radius, and r_c is the anode vane radius [5].

The second condition for magnetron operation is the synchronous condition, which states that for a slow-wave structure the phase velocity of the propagating wave of interest will equal the electron drift velocity given by

$$v_{Phase} = \frac{\omega}{k} = v_\theta \qquad\qquad \text{Equation 2.2.3}$$

where v_{phase} is the phase velocity of the wave for a RF field of frequency ω and wavenumber k. This resonant state is described by the B-H condition, which gives the maximum magnetic field that will result in stable oscillation for a given mode, expressed by

$$B_{BH} = \frac{mc^2n}{|e|\omega_n r_a d^*}\left(\frac{|e|V}{mc^2} + 1 - \sqrt{1 - \left(\frac{r_a\omega_n}{cn}\right)^2}\right) \qquad\qquad \text{Equation 2.2.4}$$

where $\omega_n = 2\pi f$ is the frequency of the mode of interest, and n is the magnetron mode number. A graphical representation of the B-H and Hull cut-off conditions can be seen in Fig. 2.1.
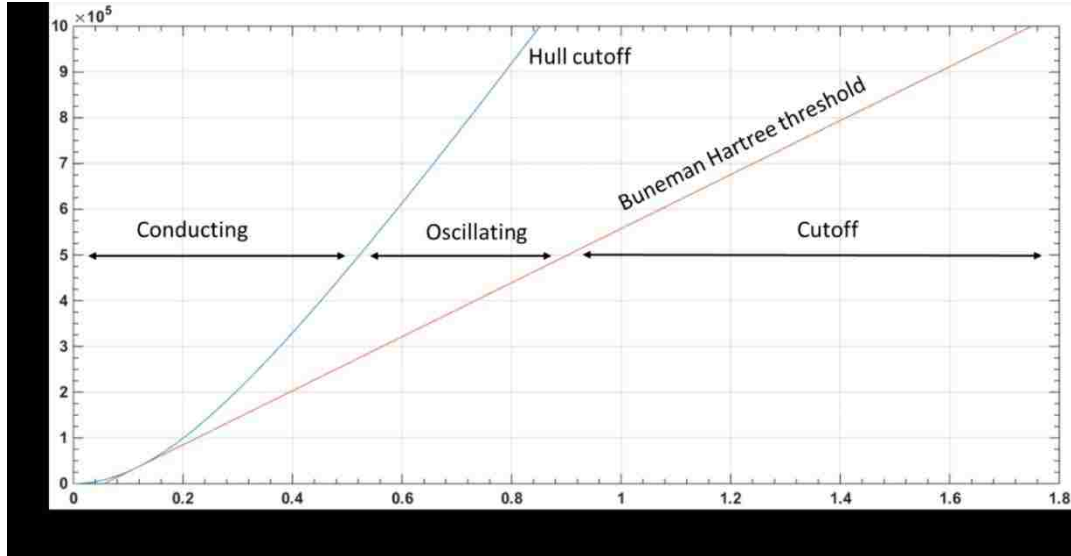
Figure 2.1 The Hull cutoff and Buneman-Hartree curves, illustrating the region of operation for a magnetron operating in the π-mode.

2.1.3 Magnetron Operating Modes and Dispersion Diagram

The synchronous condition for magnetron operation is satisfied when $v_{Phase} \approx v_{drift}$. This is accomplished by a slow wave structure constructed from cavities in the anode block. The magnetron geometry and operating conditions (applied voltage and magnetic field) will favor the growth of a particular mode from the background noise seeded by the rotating electron cloud. When the amplitude of the RF electric field for the mode of interest becomes sufficiently strong, the tangential component of the RF electric field leads to modulation of the electron cloud, which leads to spoke formation. When this occurs, the electron potential energy is transferred to the electromagnetic energy of the synchronous mode. These modes are described by the mode number n, which is the number of times the azimuthal RF electric field pattern repeats during one revolution around a magnetron. In a magnetron with N cavities, the angular spacing between cavities is given by $\Delta\theta = 2\pi/N$, with the phase shift between adjacent cavities for the nth order mode given by $\Delta\theta = 2\pi n/N$. For example, in a magnetron the two common modes are π-mode, where the RF fields are $180°$ out of phase in adjacent cavities, and 2π-mode, where the RF fields are in phase, as shown in Fig. 2.2.

These electromagnetic modes for the 6 cavity A6 magnetron, with a cathode radius of $r_{cathode}$ = 1.58 cm, an anode radius of r_c = 2.11 cm, and an anode block radius of r_a = 4.11 cm, occur along a characteristic dispersion relation curve. Figure 2.3 shows the frequency versus the phase shift plot for the standard A6 magnetron. The frequency of these modes are given by

$$f_n = \frac{\omega_n}{2\pi} \approx \frac{c}{4L_a}$$

<div align="right">Equation 2.1.5</div>

where ω_n is the angular velocity of the RF mode, c is the speed of light, and $L_a = r_a - r_c$; as mentioned earlier, the phase shift between cavities is given by $\Delta\theta = 2\pi n/N$, where N is the number of cavities, and n is the mode of interest [5], [18].

The dispersion diagram in Fig 2.3 shows the discrete oscillation frequencies supported by the A6 magnetron for one period of the first two passbands. Oscillations can occur when the beam line intersects a TE mode. We can see from Fig 2.3 that the lowest order non-degenerate mode is the π-mode, and it would be expected that the A6 magnetron would favor this mode. However, experimentally it has been shown that the A6 prefers the 2π-mode, but it can be forced to oscillate in the π-mode by means of straps or by tuning the magnetron A-K gap [11].
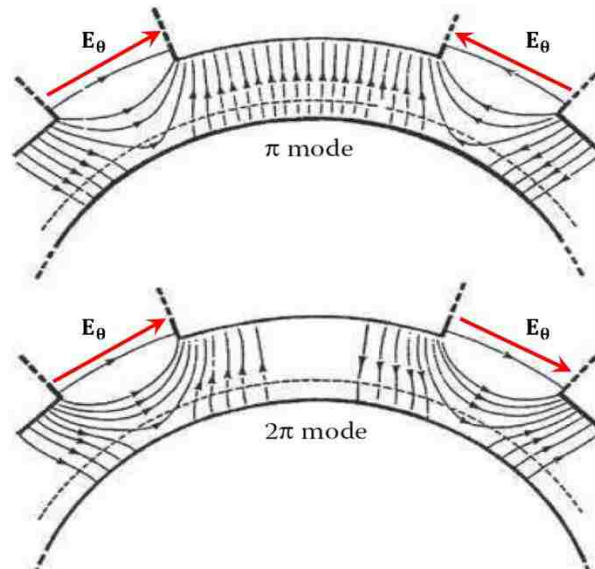
Figure 2.2 The azimuthal RF electric field distribution in adjacent cavities for the π-mode (top) and 2π-mode (bottom) [18].
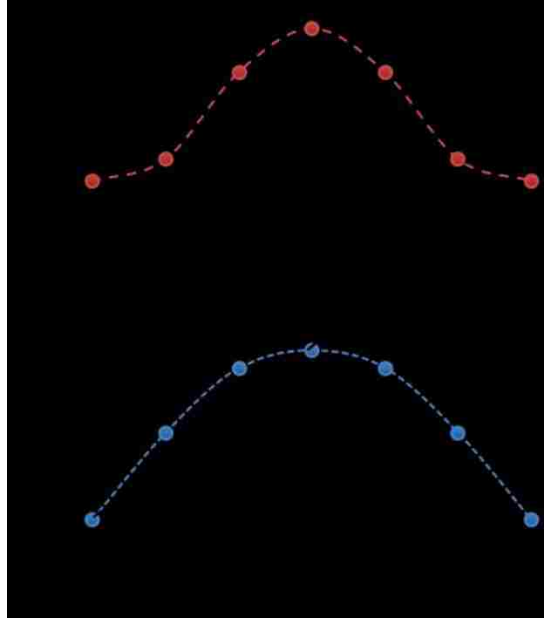
Figure 2.3 Dispersion relation of the first two passbands for the A6 relativistic magnetron. The black dashed line is the intersection of these bands with the phase velocity [5].

The common operating modes in a magnetron are the π and 2π-modes, which in a 6-cavity magnetron would form three and 6 spokes respectively. Other degenerate modes can also exist, for example the $\frac{2\pi}{3}$ and $\frac{4\pi}{3}$ modes, but they are not desirable. Figure 2.4 shows the electron spokes for these modes.

For the π-mode, the electric field in adjacent cavities is 180° out of phase, as shown in Fig. 2.4 (B). For the 2π-mode, the electric field is in phase in all the cavities, as shown in Fig. 2.4 (D). The degenerate mode $\frac{2\pi}{3}$ has the electric field distribution shown in Fig. 2.4 (A). Furthermore, the degenerate $\frac{4\pi}{3}$ mode is shown in Fig. 2.4 (C).
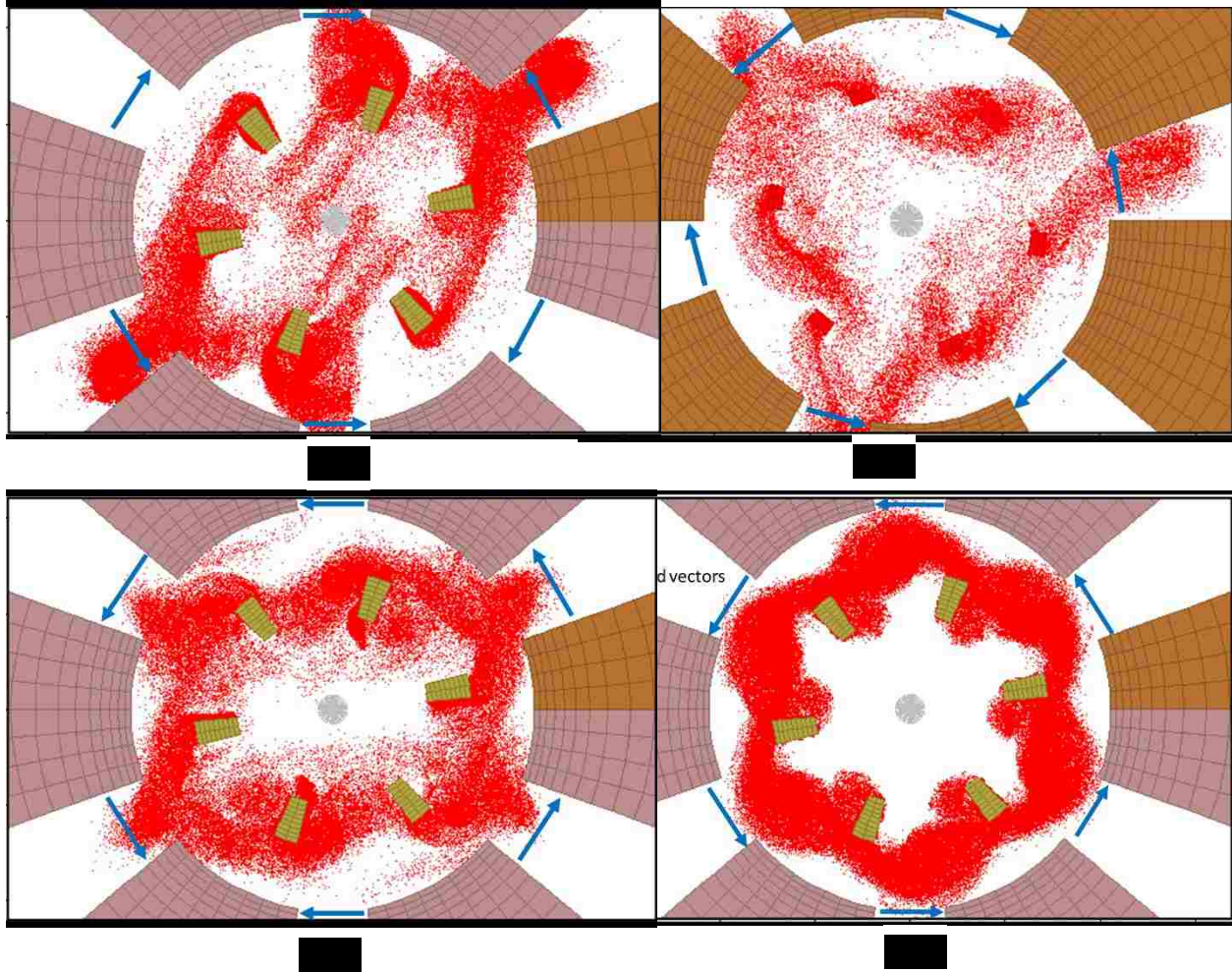
Figure 2.4 (A) is the electric field distribution and corresponding electron spokes for the 2π/3 mode; (B) is the π-mode; (C) is the 4π/3-mode; and (D) is the 2π-mode.

2.3.1 Mode Converter

In this work, a simple mode converter is proposed which converts a circular waveguide TE_{31}-mode into a TE_{11}-mode that has a Gaussian like profile [14], [15]. The field distribution of a TE_{11}-mode in a cylindrical waveguide, as well as the Gaussian distribution of the electric field, can be seen in Fig. 2.5. The Gaussian distribution of the TE_{11}-mode is especially useful for directed energy weapons applications because the maximum amplitude of the electric field is

found on axis. This field distribution allows for higher power on target, simple aperture antenna designs, and beam steering [5].
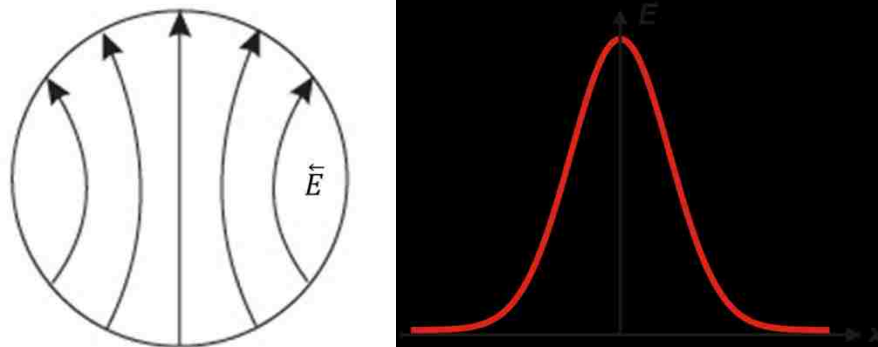
Figure 2.5 The distribution of the electric field in a cylindrical waveguide for the TE_{11}-mode (left), and the Gaussian distribution of the same electric field (right).

In recent studies performed at UNM, the original magnetron with diffraction output (MDO) [6] design was optimized, and a maximum electronic efficiency of ~70% was achieved [9]. In the MDO, the anode vanes and cavities are tapered outward radially at an optimal angle in the form of a conical horn antenna, until a final radius is reached that allows the modes of interest to be successfully radiated. Since this scheme extracts microwaves axially, the microwave window needs to be protected from leakage electrons streaming from the interaction space along the magnetic field lines, which requires a rather large beam dump. A simple illustration of the MDO and leakage electrons is shown in Fig. 2.6.

The MDO design yields a very high electronic efficiency and is capable of radiating various modes at the cost of a larger system size. The mode converter proposed in this research offers several advantages, its compactness being one of the main features. Figure 2.7 shows the schematic of the compact magnetron with simple mode converter.
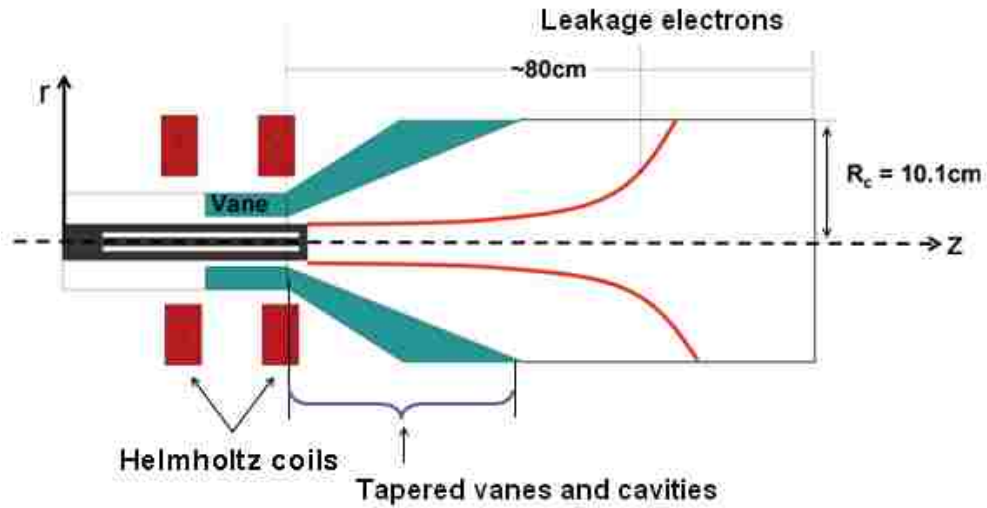
Figure 2.6 Schematic of the MDO. Leakage electrons from the interaction space are dumped onto a cylindrical waveguide before the microwave window.
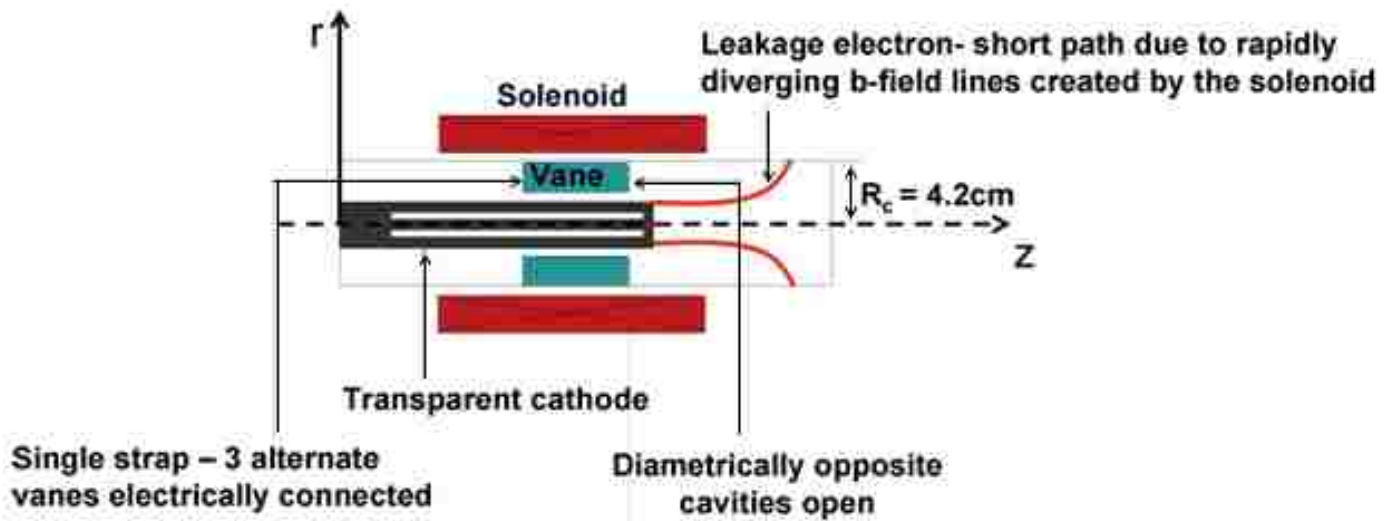
Figure 2.7 Schematic of the compact magnetron.

The concept of a simple mode converter implemented in this research is similar to ones previously demonstrated [19], where the microwaves are extracted axially through a cylindrical waveguide by opening the diametrically opposite cavities whose electric field distribution corresponds to the polarization of the TE_{11}-mode. In order to successfully radiate a Gaussian like TE_{11}-mode, the following conditions must be satisfied:

1. The magnetron has to oscillate in the π-mode, where the electric field profiles in alternating cavities are 180° out of phase.

2. The frequency of the radiated wave has to be greater than the cutoff frequency of the cylindrical waveguide.

Figure 2.8, below, shows the electric field profile of the π- mode and the corresponding mode converter designs with two or four diametrically opposite cavities opened in an A6 magnetron.
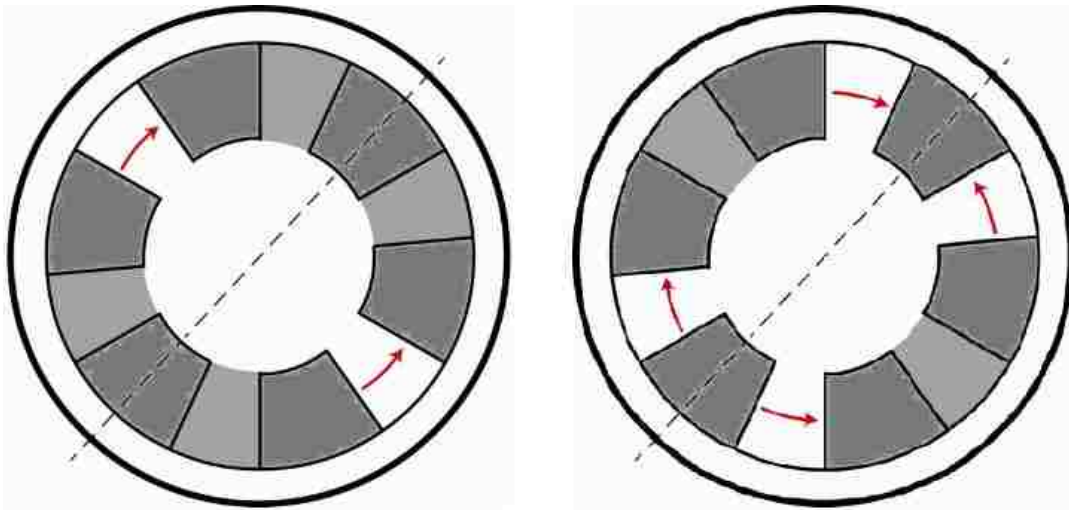
Figure 2.8 The two cavity mode converter (left) and the four cavity scheme (right), with the electric field distribution within these diametrically opposed cavities [15].

The mode converter openings must be symmetric about a line of symmetry which segregates the magnetron into identical halves, such that the cavity field components of the opened cavities are perpendicular to this line. For a 6 cavity magnetron this allows for two possible mode converter schemes, a two cavity design and a four cavity design, which can be seen in Fig. 2.8. In these figures, the dark grey signifies the location of the magnetron vanes, the

light grey signifies the location of cavity fields that are suppressed by the mode converter, the white slots represent the cavities and other areas that are not suppressed by the mode converter, and the red arrows are the electric field polarization of the cavities in the π-mode. It is to be expected that the mode conversion efficiency would be greater for designs with a greater number of opened cavities.

The mode converter is fabricated out of a thin metal plate and attaches directly to the downstream vanes of the magnetron, as shown in Fig. 2.9. This has the effect of shorting several of the cavities, causing the magnetron to favor a mode other than the π-mode. This issue can be mitigated by choosing a smaller cathode radius that favors π-mode operation. Moreover, the use of an upstream strap can force the magnetron to operate in the π-mode.

Extensive simulations were performed to verify the concept of the simple mode converter. These are discussed in detail in Chapter 3. It is noteworthy that the cathode used in this study was a 6-strip transparent cathode. It was chosen for its many advantages over other cathode designs [20].
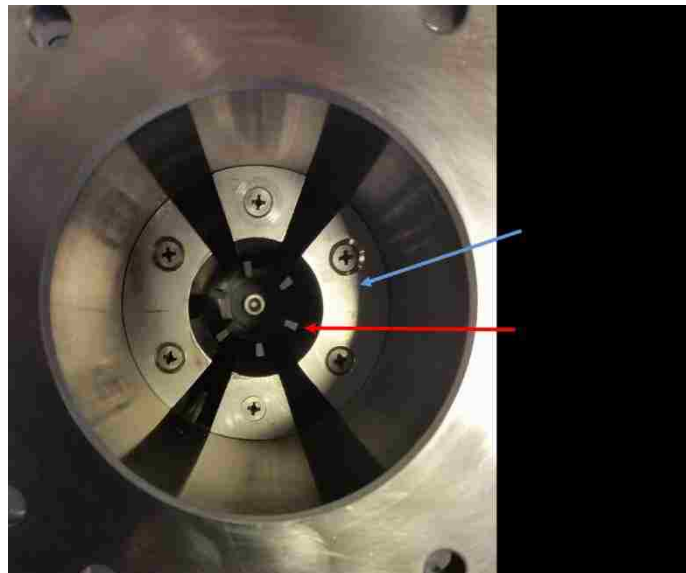
Figure 2.9 Photograph of the mode converter with the transparent cathode.

Chapter 3

Simulation Setup and Results

This chapter details the simulation efforts involved in optimizing the compact A6 magnetron with simple mode converter. Discussed herein is a brief description of the software used, the simulation setup, considerations to optimize the simulations, and finally the results of the simulations.

3.1.1 Description of MAGIC

MAGIC is a three-dimensional, fully electromagnetic and fully relativistic, particle-in-cell (PIC) code. MAGIC utilizes a Finite-Difference Time-Domain solver (FDTD) [21] in which the problem is divided into finite grids. The numerical solution is calculated by solving Maxwell's equations for each grid cell, and stepping through the grid with a time step which is determined by the gridding of the overall problem. MAGIC is capable of adaptive gridding, which allows the user to specify finer gridding in regions which require a higher degree of resolution. Beginning from a specified initial state, the code simulates a physical process as it evolves in time. The full set of Maxwell's time-dependent equations is solved to obtain the electromagnetic fields. Similarly, the complete Lorentz force equation is solved to obtain the relativistic particle trajectories, and the continuity equation is solved to provide current and charge densities for Maxwell's equations [22]. This provides the self-consistent interaction between the fields and particles. MAGIC is ideal for modeling complex geometries, material properties, ionization of gaseous media, and emission processes, as well as interactions between waves and particles.

3.2.1 Simulation Setup

The setup for the simulation is shown in Fig. 3.1. From this figure we can see the various diagnostic areas, as well as the input and output ports of the magnetron. The input power of the magnetron is injected via the input port, which feeds a short coaxial section with a voltage pulse amplitude of 350 kV, a duration of 30 ns, and a risetime of 2 ns.
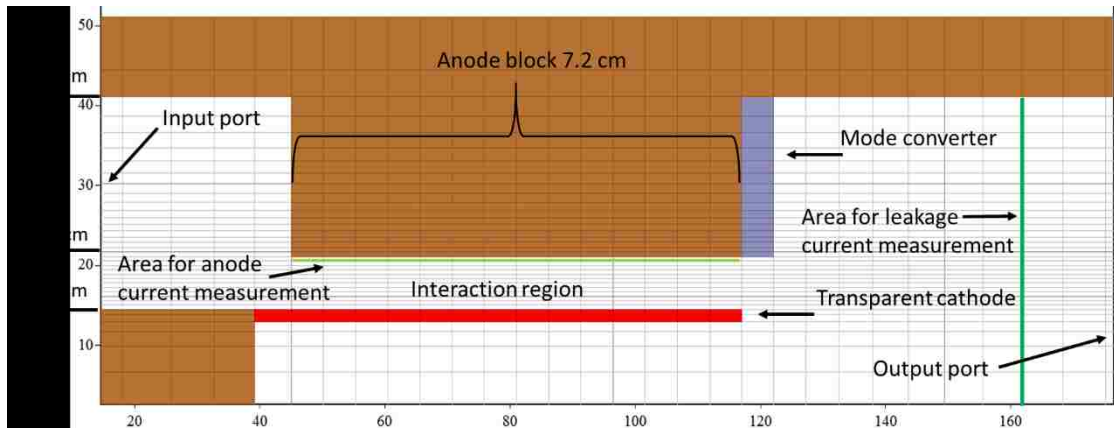
Figure 3.1 The compact A6 magnetron viewed from the r-z plane.

The emission process used for the diode is the explosive emission model in MAGIC. This ensures that the electrons are emitted at the cathode surface when the normal electric field reaches a specified value of 100 kV/cm. The magnetic field is defined using a function which keeps the axial magnetic field constant at a specified level throughout the interaction space, and diverges very rapidly to the waveguide wall. This function closely approximates the magnetic field generated by a solenoidal coil.

The current diagnostic shown in Figure 3.1 measures the total current flowing from the cathode to the anode by defining a cylindrical surface in the r- θ plane, which is arbitrarily close to the anode. This area encompasses the entire interaction region, and measures the current as it passes through. Additionally, the downstream leakage current is measured by creating an area in the r-θ plane downstream of the slow wave structure. The RF measurements are made at the output port, shown in Fig. 3.1. The port command in MAGIC [22] allows the RF to leave the defined area, but does not allow any reflections to reinter the port. From these observations we can discern the output power, operating frequency, and the TE_{11}-mode pattern.

3.2.2 Convergence Test

The accuracy of the MAGIC simulations is highly dependent on the gridding of the simulation volume. This is due to how the FDTD algorithm progressively solves for the field quantity in the grid cells. Additionally, the duration of the simulation is determined by the time step, which is calculated based on the number of grid cells contained in the simulation volume.

19

As such, it is very important to build the simulation file with proper gridding. In order to ensure that proper gridding was used, a convergence test was performed [23].

The majority of the physics which requires a high degree of resolution occurs within the interaction region. A convergence test was performed by varying the radial grid within this region from 10 to 25 grids, while the azimuthal and axial gridding were held constant at 5 degrees and 5 mm, respectively. The axial and radial grid resolution in the interaction space can be seen in Figs. 3.2 and 3.3.
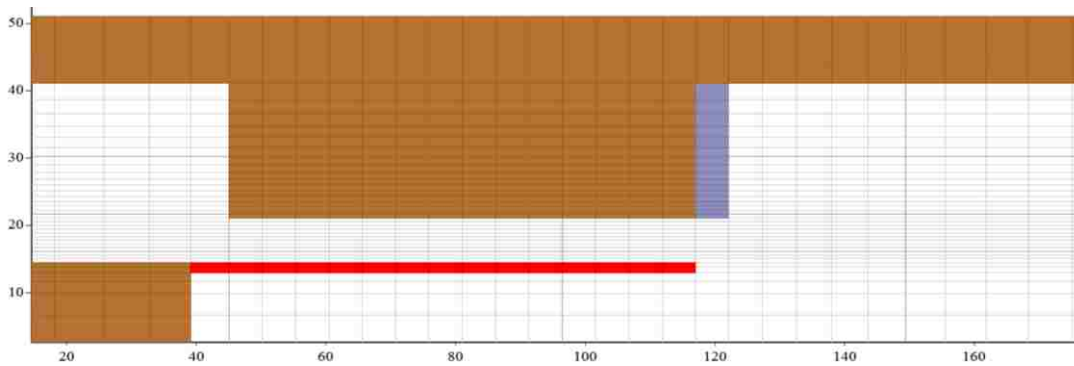
Figure 3.2 Spatial grid resolution in the r-z plane.
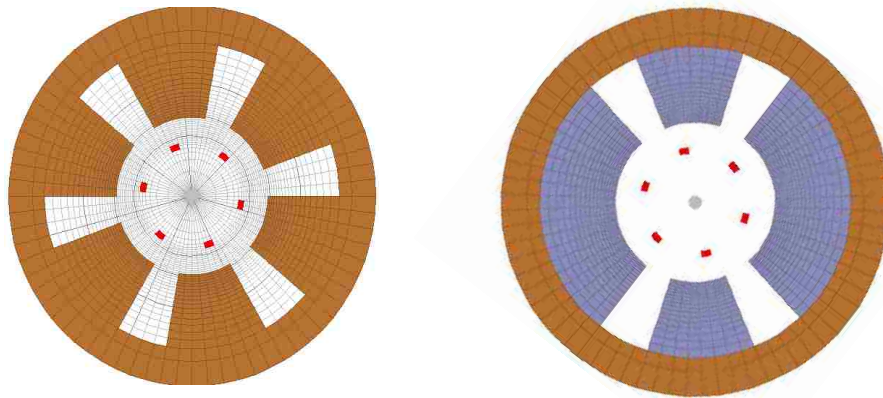
Figure 3.3 (Left) is the A6 magnetron viewed form the r-θ plane. (Right) is the A6 magnetron viewed form the r-θ plane, showing the mode converter attached to the downstream end of the anode vane.

20

The convergence test simulations were run with the same input voltage and magnetic field parameters, and the output parameters, such as the anode and leakage current, frequency, and total output power, were recorded. By comparing the results, we determined the acceptable gridding for the interaction region of the magnetron.

Figure 3.4 shows the time dependence of microwave output power for various radial grid resolutions, and shows that the final saturation power was approximately the same for all the cases, with some differences in the risetimes. Since these results exhibit very similar behavior, the rest of the simulations were conducted at 10 grid radial resolution to save time.
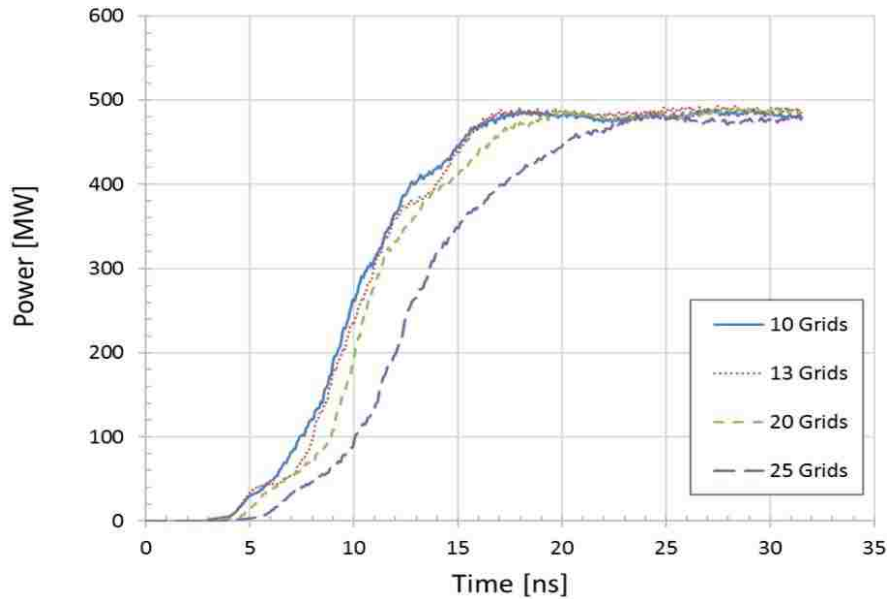
Figure 3.4 The radiated power for the four spatial grid regimes of 10, 13, 20, and 25 grids.

3.2.3 Cathode Length Optimization

As discussed in Chapter 2, in order for the mode converter to radiate a TE_{11}-mode it is necessary for the magnetron to oscillate in the π-mode. Additionally, to provide maximum conversion efficiency, it was necessary to optimize the radius and the length of the emission region of the cathode. The cathode radius was chosen to be $R_c=1.45$ cm. This value was determined through simulation, by varying the radius and performing a B-field sweep at each new radius value. The input parameters for these simulations were held constant, and the output

parameters, such as the output power, power saturation time, π-mode electron spoke formation, and the range of B-fields for which the π-mode was observed, were considered. This led to the conclusion that a cathode radius of 1.45 cm is ideal for B-fields ranging from 0.50 T to 061 T.

The transparent cathode used for the radial extraction A6 magnetron consists of cathode strips which extend past the slow wave structure, as well as a cylindrical ring at the end of the cathode designed to reduce the leakage current. However, it was noticed that using this cathode design resulted in decreased output power, and led to mode competition [11]. Therefore, cathode length optimization was conducted. It was found that the π-mode operation was enhanced and the microwave output power reached 500 MW when the cathode strips were flush with the end of the anode block. The power dropped to 100 MW and 60 MW when the cathode strips extended ±1 cm past the anode block, respectively. The result of this optimization is shown in Fig. 3.5.

Furthermore, it was found that the upstream end of the cathode strips needed to start at or slightly before the edge of the anode block for stable behavior. The results of this parameter sweep are shown in Fig. 3.6. The cathode for experimentation was manufactured based on these results.
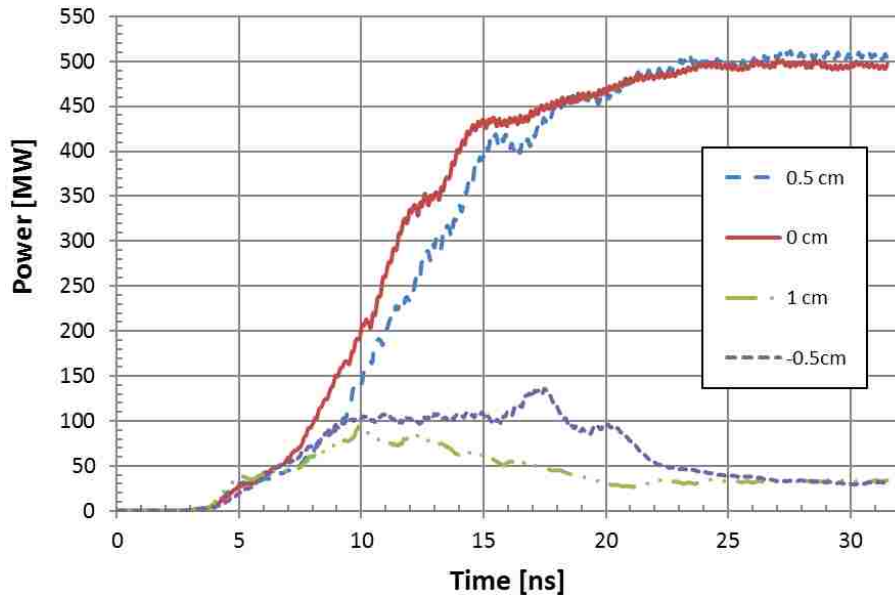
Figure 3.5 The output power of the compact magnetron as the downstream cathode strips are varied in increments of 0.5 cm.
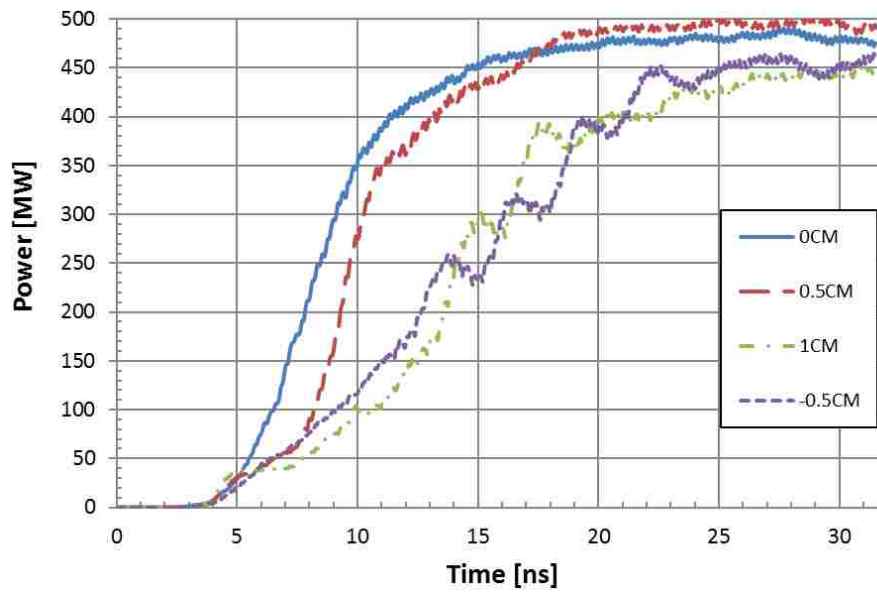
Figure 3.6 The output power of the compact magnetron as the upstream cathode shank is varied in 0.5 cm increments.

3.3.1 Simulation Results

Figure 3.7 is the power and frequency dependence on the applied magnetic field. It can be seen that over the magnetic field range of 0.51 T to 0.61 T the magnetron oscillates at a single frequency with an output power greater than 400 MW.
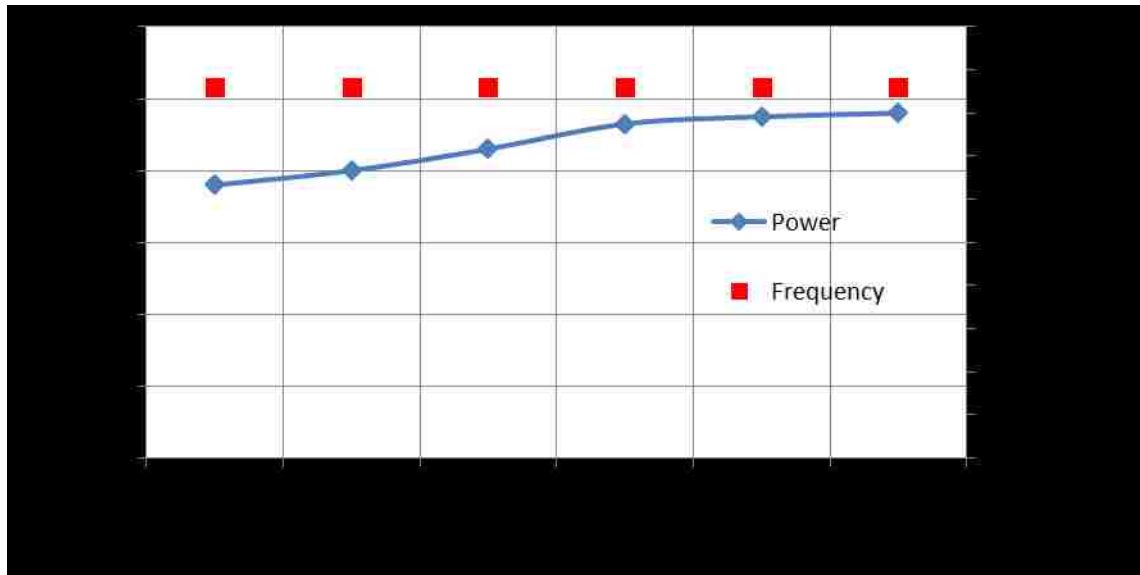
Figure 3.7 The power and frequency dependence on the applied magnetic field.

Figure 3.8 shows the anode and leakage current with relation to time for an applied magnetic field of 0.61 T. The anode and leakage currents saturate at 11 kA and 4 kA, respectively. Figure 3.9 shows the microwave output power, along with the RF electric field and its corresponding Fast Fourier Transform (FFT). The microwave power reaches saturation in 15 ns, with an amplitude of 480 MW at 2.43 GHz. Figure 3.10 displays the electron spokes in the magnetron confirming π-mode operation, as well as the electric field contour and vector plots measured at the output port. This indicates the TE_{11}-mode, with some angular polarization. Plots were recorded for a complete period to verify that the mode was not a rotating mode.
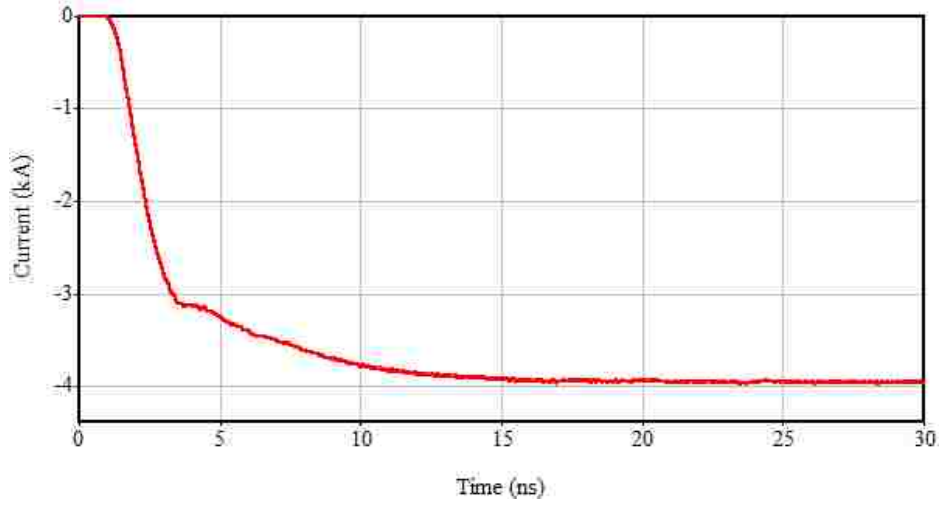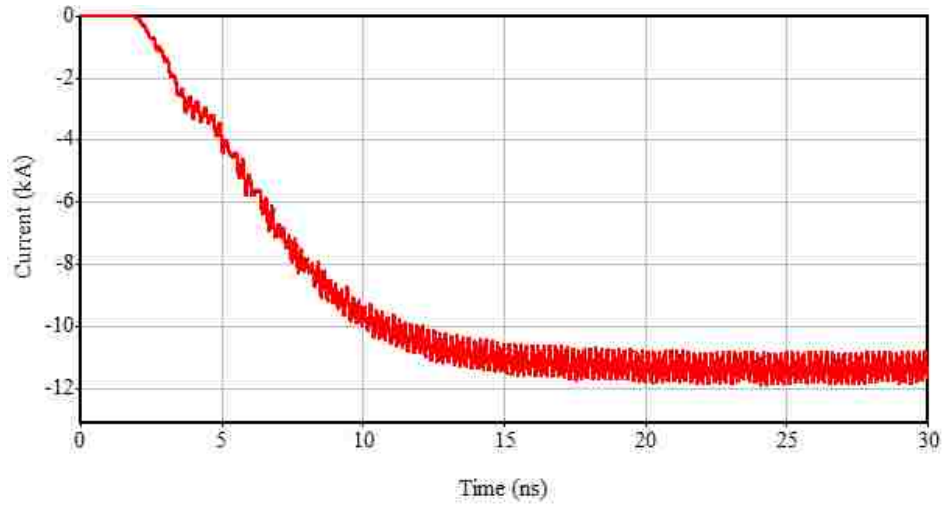
Figure 3.8 Anode (top) and leakage current (bottom) vs. time with an applied magnetic field of 0.61T and voltage of 350 kV.
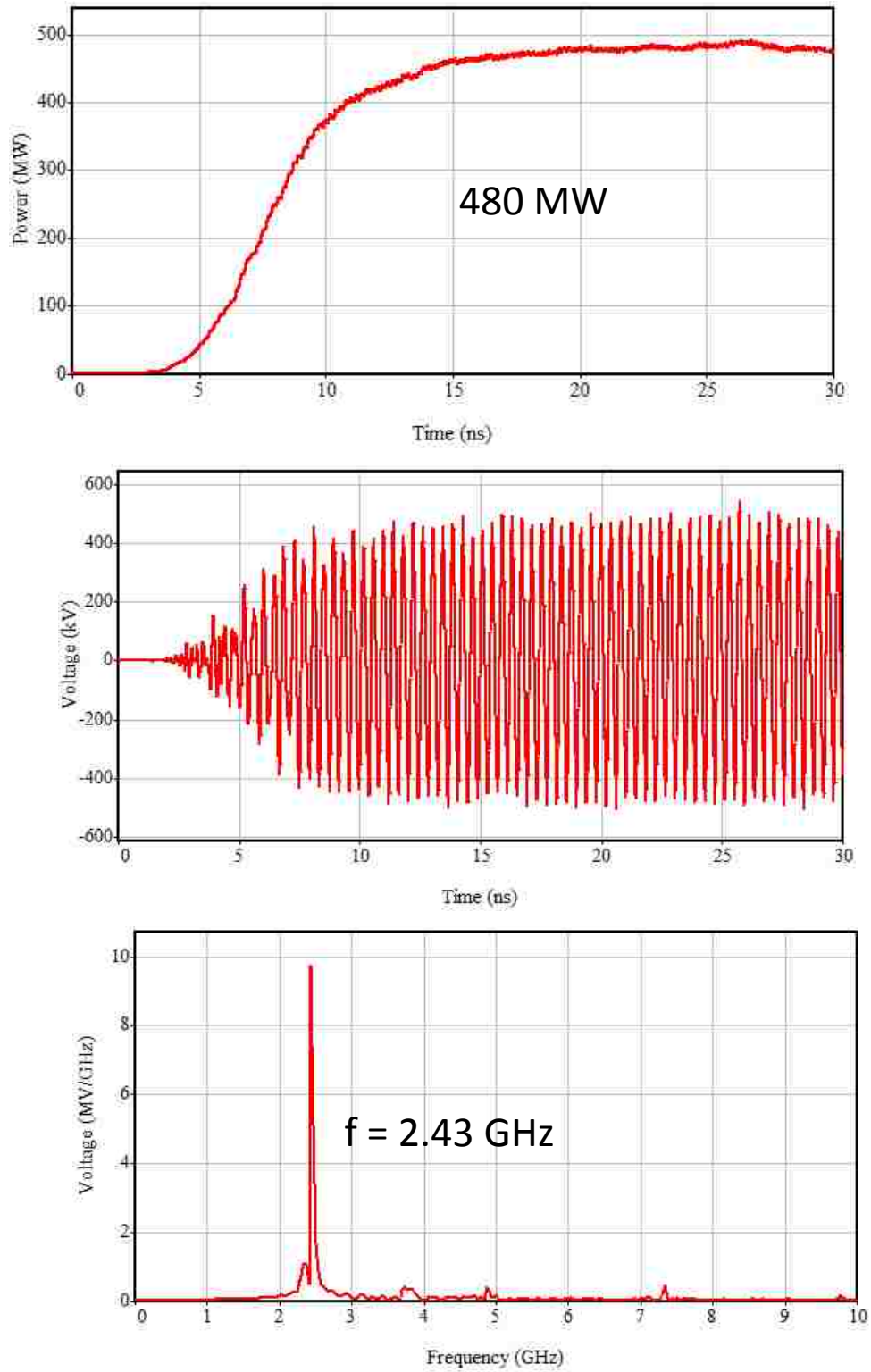
Figure 3.9 Output power vs. time (top), RF envelope (middle), and FFT (bottom) at an applied magnetic field of 0.61 T and voltage of 350 kV.
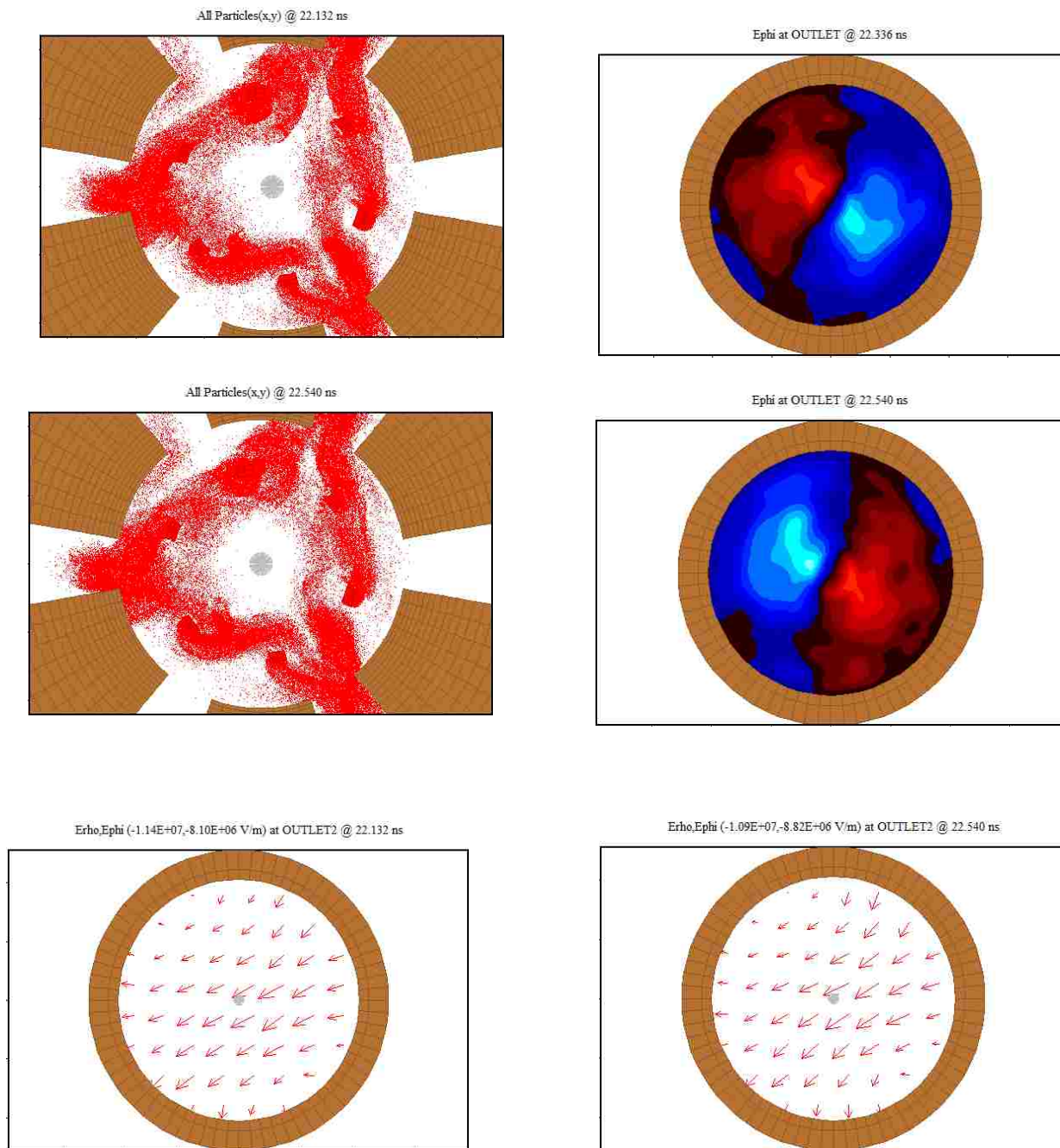
Figure 3.10 The electron spokes (top left) and contour plot showing the TE$_{11}$ output mode (top right). (Bottom) is the vector plot also illustrating the TE$_{11}$-mode.

Chapter 4

Experimental Setup

This chapter details the experimental setup used for the verification of the compact A6 magnetron with simple mode converter. The PULSERAD accelerator and its constituents are discussed, as well as the diagnostics and peripherals needed for these experiments.

4.1.1 PULSERAD-110A

The PULSERAD PI-110A accelerator, manufactured by The Physics International Corporation, is a Marx bank pulser that has been redesigned to provide a 350 kV, 30 ns voltage pulse with a risetime less than 4 ns into a 20 Ω load [24]. Simulations have shown that long voltage risetimes in relativistic magnetrons can lead to mode competition and decreased output powers, as shown in Fig. 4.1. This results from the synchronous condition (Buneman-Hartree) for various modes being satisfied during the risetime of the voltage front. The self-excitation of oscillations in resonant microwave sources strongly depends on the relation between the cavity fill-time t_s of the sth mode, and the voltage risetime t_v [25], or, more correctly, on the time of increasing azimuthal electron drift velocity as the voltage grows. For the π-mode and 2π-mode of the A6 magnetron, $t_s \approx 4 - 5$ ns [20]
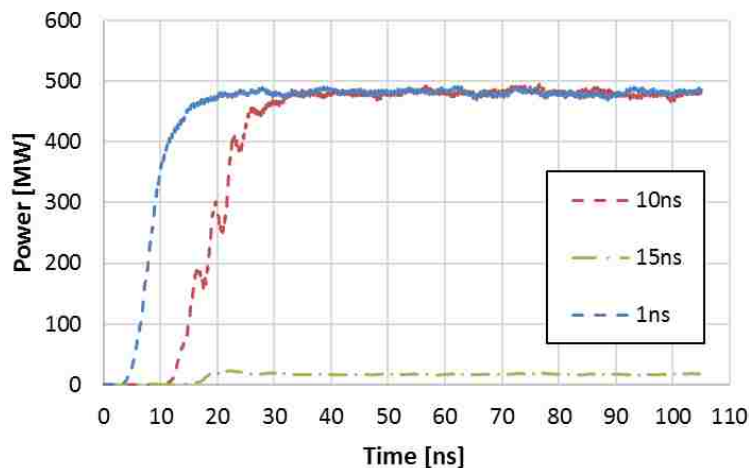
Figure 4.1 The MAGIC results for the output power of the compact magnetron with simple mode converter for input voltage risetimes of 1 ns, 15 ns, and 20 ns.

Figure 4.2 is the schematic of PULSERAD, which consists of a 6-stage Marx that charges a 20 Ω, 30 ns coaxial pulse forming line (PFL) followed by a self-break oil switch, which discharges into a 20 Ω transmission line. In the following sections the components of PULSERAD will be discussed.

4.1.2 Marx Bank

The circuit diagram for the Marx bank, as well as a photograph of the Marx during routine maintenance can be seen in Fig 4.3. The Marx bank consists of 6 bipolar, 0.050 µF case-center-grounded capacitors, which are charged in parallel to ~±20-35 kV and discharged in series via 7 gas switches pressurized with SF_6. The switches on the first three stages are externally triggered by means of a 50 kV pulse delivered by an external krytron trigger circuit. When the Marx is triggered, the negative voltage output of the Marx feeds directly into a 7 Ω $CuSO_4$ (copper sulfate) resistor and a 20 Ω coaxial PFL.
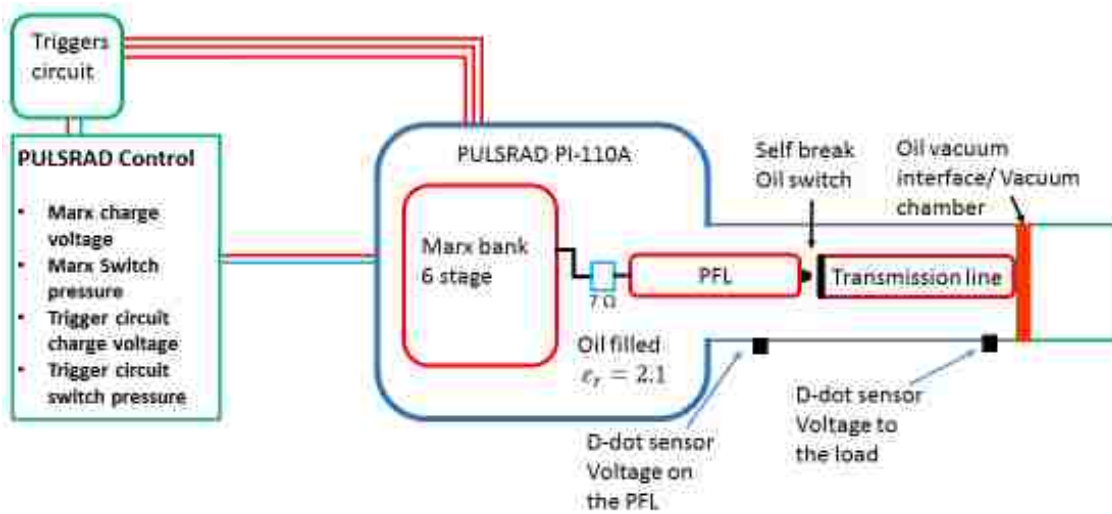
Figure 4.2 The breakdown of the PULSERAD accelerator and its charging system.
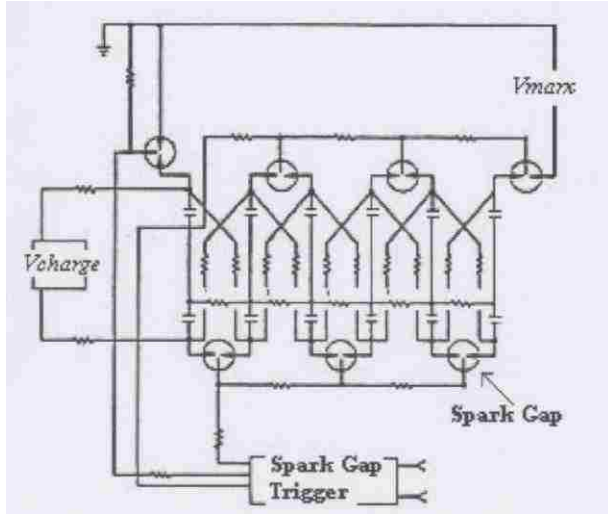
Figure 4.3 An equivalent circuit diagram of the Marx bank (left), and a photograph of the Marx bank being maintained before installation in the accelerator (right).

PULSERAD is designed to provide a ringing gain of 1.74 by making the Marx capacitance greater than the PFL capacitance. When this condition is met, the voltage delivered to the PFL will be roughly 1.74 times that of the Marx discharge voltage, as shown in Equation 4.1.1.

$$V_{pfl} = V_{marx}(\frac{C_m}{C_m + C_{pfl}})(1 - \cos(\omega t)) \qquad \text{Equation 4.1.1}$$

Here V_{pfl} is the voltage on the Pulse Forming Line (PFL), V_{marx} is the discharge voltage of the Marx bank, $C_m = 8.33$ nF is the equivalent series capacitance of the Marx bank, and $C_{pfl} = 1.2$ nF is the capacitance of the coaxial PFL. We can see from Equation 4.1.1 that when the cosine term is -1 and the ratio of the Marx capacitance to PFL capacitance is 0.871 this leads to a maximum gain factor of 1.74. The discharge voltage is determined by the oil switch gap. The self-break oil switch design is discussed in the next section.

4.1.3 The 2 ns Self-Break Oil Switch

In order to achieve a voltage pulse with a risetime less than the fill-time of the magnetron (which is about 7-8 ns), a low-inductance peaking switch was designed. This switch was designed as a spherical point to plane self-break switch immersed in oil which has a dielectric constant of $\varepsilon_r = 2.1$. This design is crucial for limiting the inductance, and subsequently the risetime, of the switch channel by ensuring only one breakdown path forms. A diagram of the oil switch can be seen in Figure 4.4.
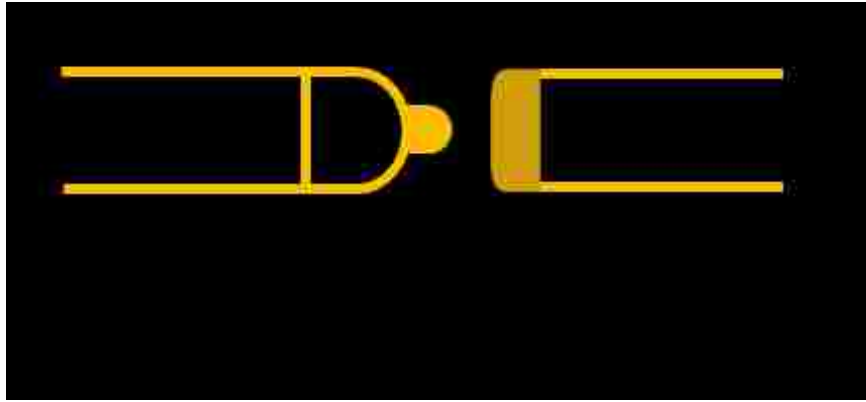
Figure 4.4 The low-inductance self-break oil switch design. The spherical electrode is affixed to the PFL while the transmission line has a smooth planar surface.

The risetime of the switch can be determined by equations 4.1.2-4.1.5.

$$\tau_t = (\tau_R{}^2 + \tau_L{}^2)^{\frac{1}{2}}$$ Equation 4.1.2

where τ_t is the total risetime, τ_R is the time for the resistive phase of the switch, τ_L is the inductive contribution to the risetime given by

$$\tau_R = \frac{5}{(NZE^4)^{\frac{1}{3}}}$$ Equation 4.1.3

$$\tau_L = \frac{L}{NZ}$$ Equation 4.1.4

$$L = 2d\ln\left(\frac{b}{a}\right)$$ Equation 4.1.5

Here N is the number of channels (1), Z is the impedance of the driving circuit (40 Ω), E is the mean electric field (980 kV/cm), L is the inductance per switch channel, d is the switch gap

(roughly 0.61 cm), a is the radius of the channel (0.01 cm), and b is the radius of the disc feeding the channel (0.005 cm). This leads to a 10-90% risetime $\tau_t = 3.5$ ns [24].

The gap of the oil breakdown switch is externally adjustable via an O-ring-sealed wrench. The gap adjustment was designed on a 1:1 turns ratio, meaning one full turn of the wrench translates to one turn of the PFL electrode. As the PFL electrode rotates, it moves in or out at a rate of 14 threads per inch, or 1.814 mm per turn of the wrench. Additionally, the electrode's maximum extension is 25.40 mm (1 inch), and its minimum extension is 15.60 mm (0.614 inches) [9].

The oil switch was designed to give a voltage pulse with a risetime of less than 4 ns. In order to characterize the of self-break switch design, a switch calibration was performed. This was accomplished by replacing the magnetron load with a 20 Ω copper sulfate resistive load. Figure 4.5 is a photograph of the oil switch during this switch characterization.

Figure 4.5 Photographs of the 2 ns self-break oil switch during switch characterization. Looking though the view port before firing (left), and during firing (right).

To determine the risetime of the oil switch, D-dot sensors were used to capture the voltage waveforms during testing. These waveforms are shown in Fig. 4.6. Additionally, the 10-90% risetime of the load voltage shows a ~2 ns risetime into a matched resistive load.
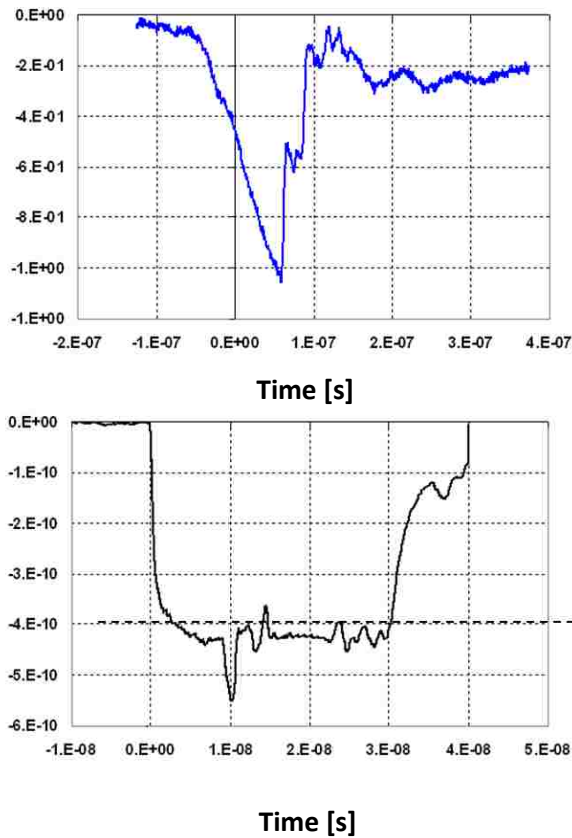
Figure 4.6 Plot of the voltages measured from the D-dot probes. (top) is the upstream D-dot probe (voltage of the PFL), and (bottom) is the downstream D-dot probe (voltage on the load).

4.2.1 Electromagnetic Circuit

The pulsed electromagnet circuit was designed and constructed to provide the external insulating magnetic field required for crossed-field operation of the magnetron. This system was designed to power a Helmholtz coil pair, which provides a high degree of uniformity of the magnetic field in the magnetron interaction region. The Helmholtz coil configuration is two identical coils connected in series, where the average distance between the coils is equivalent to the average radius of the coils. For the radial extraction magnetron, this spacing between the coils is needed to accommodate the output waveguide. [11]

The pulsed electromagnet circuit was designed to switch a 3 kV, 1.6 mF capacitor bank capable of delivering 7.2 kJ of energy into a 2.5 mH, 7 Ω electromagnet load by means of a thyristor switch. Due to the LRC design, the current through the coils, and subsequently the

magnetic field, does not reach its peak value until 24 ms after the initial trigger signal has been sent. As such, this system was designed to be triggered 24 ms prior to the PULSERAD. The pulsed electromagnet circuit can be seen in Fig. 4.7 [9],[26].
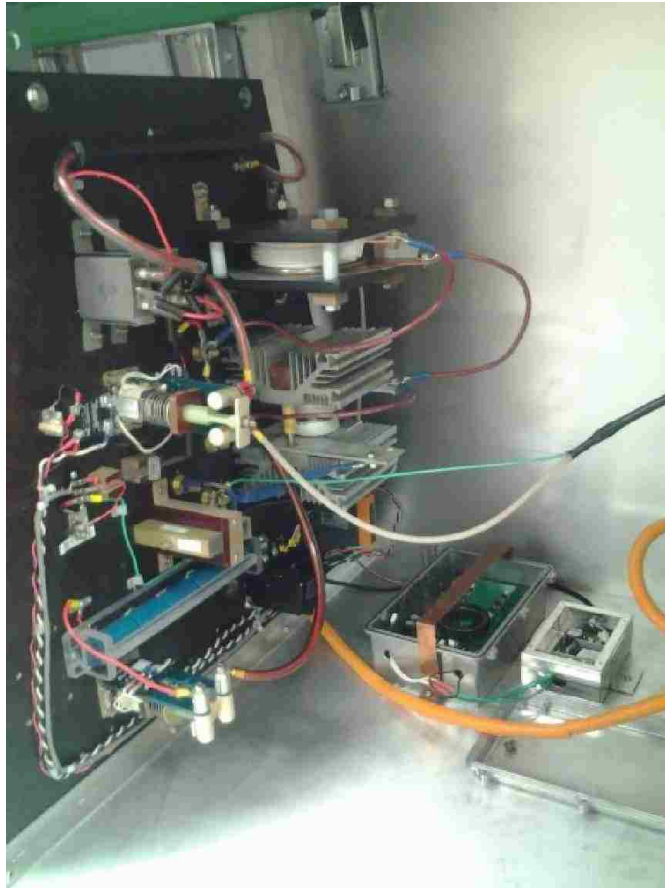
Figure 4.7. PULSERAD's pulsed electromagnet circuit.

The diagnostics of this circuit are capable of providing real-time feedback on the voltage and the current of the capacitor bank. The voltage diagnostic used was a 1000:1 voltage divider, and a precision 0.0053 Ω current viewing resister (CVR) was used measures the current delivered to the electromagnetic coils.

In order to discharge the capacitor bank into the coils, a high power thyristor switch was used. The thyristor was triggered with an optically-isolated fiber optic link to avoid triggering due to RF coupling. An additional consideration for triggering the thyristor was the input

waveform. According to information provided by the manufacturer, the trigger signal should match that of Fig. 4.8 [26], [27].

Triggering of the thyristor was accomplished with an optically-isolated transmitter and receiver. However, in order to satisfy the triggering requirements of the thyristor, a triggering circuit was designed. The current waveform needed for triggering the thyristor, in order to minimize damage while discharging a short, high power pulse, can be seen in Fig. 4.8.
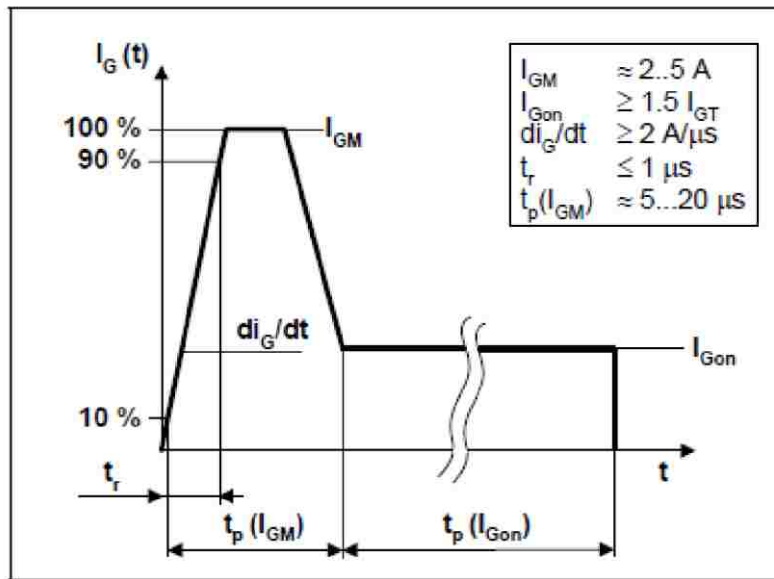
Figure 4.8 Required thyristor current waveform [27],[9].

To provide a large-magnitude short pulse followed by a small-magnitude long pulse, a compact toroid tape-wound current transformer with two primary coils, one secondary coil, and one saturation coil was used. This transformer was driven by two monostables LM555 timers, which converted the incoming optical pulse into two pulses of different lengths, which in turn activate two separate high current, 15 V MOSFET drivers. The output of the drivers was delivered to the two of the primary coils of the toroid transformer, where the signals were summed to provide the desired waveform. Additionally, a reverse saturation coil was added to the transformer to eliminate voltage sag on the output due to saturation memory of the core [26].

The secondary coil was delivered to the gate of the thyristor, discharging the 1.6 mF capacitor bank into the Helmholtz coils. For the charging of the capacitor bank, an 8 kV, 250 mA Glassman power supply was used. This power supply was voltage and current controlled and monitored via a USB2.0-boosted cable using software provided by Glassman High Voltage Inc.

4.3.1 Voltage Diagnostics

To measure the voltage at the load, as well as the voltage of the PFL, D-dot probes were implemented. These probes are imbedded in the outer conductor of the coaxial transmission line upstream and downstream of the oil breakdown switch, and measured the voltage on the PFL and the voltage supplied to the load, respectively. In Fig. 4.1 the location of the D-dot sensors can be seen [28].

Traditional D-dot voltage sensors are based on the electric field coupling principle and can be used to measure high voltage. D-dot sensors output a voltage signal that is proportional to the first-order differential component of the electric displacement current over the sensor area with respect to time ($\dot{D}$ or $\varepsilon dE/dt$). The probes used are modified N-type connectors with the center conductor extending to the inside wall of the transmission line. Additionally, these sensors were calibrated at $3.4 \times 10^{-13} [V^{-1}]$ for the PFL and $3.74 \times 10^{-13} [V^{-1}]$ for the downstream transmission line [9].

4.3.2 Current Diagnostics

In order to measure the current of the magnetron, Rogowski current sensors were used. A Rogowski coil consists of a helical coil of wire wound tightly about a non-magnetic core. This coil is then placed around the conductor for which the current measurement is to be taken as shown in Fig. 4.9. Rogowski coils are especially useful when measuring high currents on the order of 10s-100s kA. As Rogowski coils use a non-magnetic core to support the secondary windings, mutual coupling between the primary and secondary windings is weak. Because of weak coupling, to obtain quality current measurements, Rogowski coils should be designed to meet two main criteria:

- The relative position of the primary conductor inside the coil loop should not affect the coil output signal, and

- The impact of nearby conductors that carry high currents on the coil output signal should be minimal.

To satisfy the first criterion, the mutual inductance M must have a constant value for any position of the primary conductor inside the coil loop. M is given by

$$M = \mu_0 \cdot n \cdot S \qquad\qquad \text{Equation 4.4.1}$$

where μ_0 is the permeability of free space, n is the number of turns, and S is the cross-sectional area of the coil shown in Figure 4.9. This can be achieved if the windings on the non-magnetic core have a constant cross-section S, are perpendicular to the center line of the core, and have a constant turn density n. The output voltage $V_s(t)$, which is measured as a voltage drop across the resistor R_R, is proportional to the rate of change of the measured current given by [29]

$$V_s(t) = -M \frac{di_p(t)}{dt} \qquad\qquad \text{Equation 4.4.2}$$

where $i_p(t)$ is the current measured, $V_s(t)$ is the proportional differential voltage of the Rogowski, and M is the mutual inductance described in Equation 4.4.1.

The Rogowski coils that were used to measure the total and leakage currents are able to approximate a self-integrating coil, meaning the output voltage of the coil is proportional to the observed current. This was accomplished by designing the coil such that the RL time constant τ of the coil is significantly longer than the current pulse to be measured, $\tau = \frac{L}{R}$. This leads to the simplification of Equation 4.4.2 to [11], [30]

$$V_s = \frac{i_p(t)}{n} R_R \qquad\qquad \text{Equation 4.4.3}$$

Here V_s is the voltage across the resistor R_R, n is the total number of turns, and $i_p(t)$ is the current to be measured.
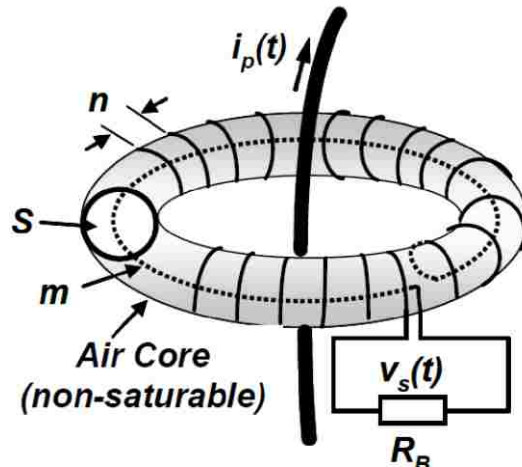
Figure 4.9 The layout of a traditional Rogowski coil.

4.3.3 RF Diagnostics

The measurements of RF frequency and pulse shape were captured with a D-band rectangular waveguide detector, which was placed in front of the horn antenna. The signal was coupled out of the waveguide into a RG-241 cable by a waveguide-to-coax adapter. From this measurement we could determine the duration of the RF pulse, as well as the frequency by applying a Fast Fourier transform (FFT) [31]. For the mode diagnostic, a neon bulb array was used. This board consists of low-voltage neon bulbs arranged in a grid, which light up due to the RF electric field. The mode pattern can be photographed using an open shutter DSLR camera.

4.3.4 HPM Calorimeter

A microwave calorimeter, previously constructed for the MDO experiments, was used for power estimation. The main advantage of using a calorimeter is its ability to measure any radiated mode, even if multiple degenerate modes exist simultaneously. The calorimeter structure consists of two round sections of clear acrylic (polystyrene), which sandwich a 40 cm diameter, 0.9525 cm thick layer of pure ethanol. At the frequencies of interest, the typical power absorption coefficient was ~61%. This was calculated using two identical horn antennas and a network analyzer [9], [32].

The calorimeter operates by absorbing the microwave energy, which causes expansion of the alcohol volume. The alcohol is allowed to expand into a 1 mm glass capillary tube with two

38

parallel filaments. This causes a change in resistance that corresponds to the amount of energy deposited. This measurement can easily be converted into power by considering the duration of the RF pulse. Figure 4.10 is a diagram of the calorimeter design [33].
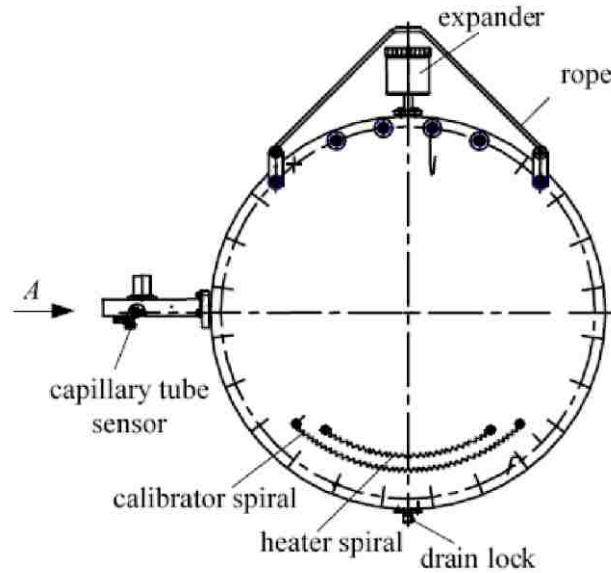
Figure 4.10 The design of the microwave calorimeter [9].

4.4.1 Magnetron and Hardware

The radial extraction A6 magnetron was manufactured out of 304 stainless steel using wire EDM techniques by a local machining company, with a tolerance of one thousandth of an inch (0.001"). For the verification of the compact magnetron with simple mode converter, which is an axial extraction schema, only minor modifications are needed, such as a cap for the radial extraction port. The simple mode converter, which was optimized through simulations, was manufactured out of 1/8" stainless steel with a precision CNC mill. Both two and four cavity extraction designs were manufactured. Details of the design for the mode converter are described in Chapter two.

Since the radius of the cathode was reduced to 1.45 cm, a cathode shank and a new cathode needed to be manufactured. The cathode shank was manufactured in-house out of stainless steel. The cathode used was the transparent cathode developed at UNM [20]. It was constructed of low-porosity, vacuum compatible POCO graphite. Graphite was the material of

choice because of its excellent field emission characteristics, small erection delay, and ease of machining. Figure 4.11 is a photograph of the finished cathode.
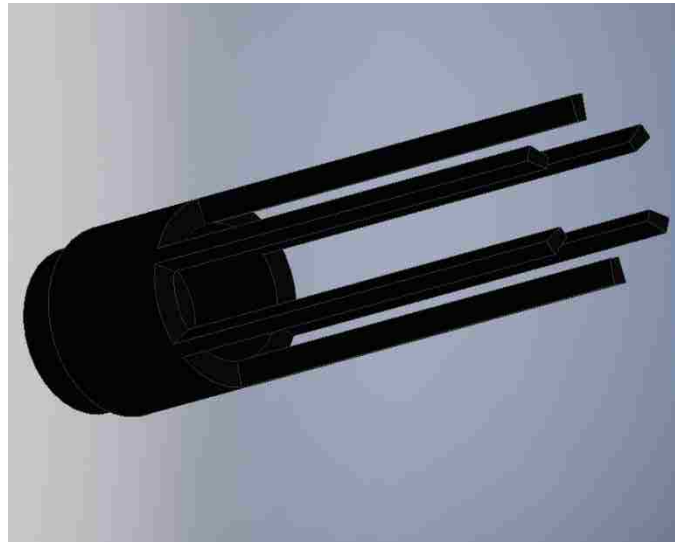
Figure 4.11 The isometric AutoCAD drawing of the transparent cathode.

4.4.2 Beam Dump

In magnetron design it is important to consider the leakage electrons and where they are dumped. This is because high-energy leakage electrons can damage the dielectric output window of the waveguide. In an axial extraction scheme such as the compact A6 magnetron, the downstream leakage current is in the range of 3-4 kA, which is sufficient energy to damage the polycarbonate window.

In order to prevent this damage, a beam dump was designed such that the leakage electrons would be deposited on the walls of a stainless steel tube. To determine the necessary length of the beam dump, FEMM, a finite element 2-dimensional magnetostatic code [34], was used to simulate the system. Figure 4.12 shows the magnetic field lines from the Helmholtz coils as they intersect with the wall of the beam dump, indicating where the electrons will be deposited. Simulations showed that the leakage electrons would deposit 21 cm downstream of the magnetron. For this reason a cylindrical waveguide with a length of 30 cm was needed to serve as a beam dump.
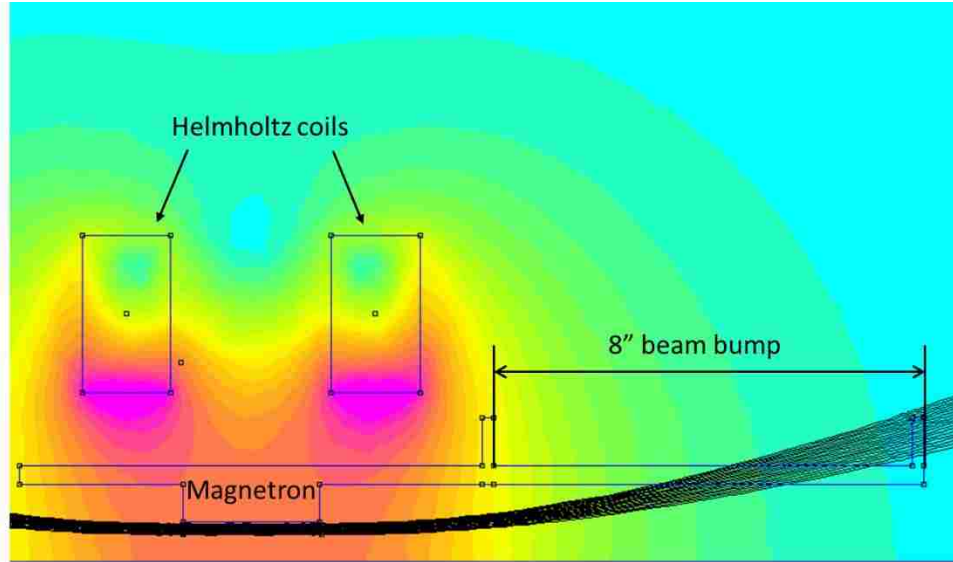
Figure 4.12 The FEMM simulation of the Helmholtz coils, showing the distance at which the electrons will be deposited.

4.4.3 Conical Horn Antenna

Horn antennas are among the simplest and most widely used microwave antennas. The antenna is needed to radiate the RF with minimal reflections due to the impedance mismatch, as well as to increase the directivity and gain of the radiation pattern. Since we used an existing antenna design, it was necessary to ensure that the output aperture could handle the power that would be transmitted. This was done by calculating the electric field at the vacuum/atmosphere aperture. This calculation can be performed using equation 4.3.1 [5]

$$P_{TE} = \frac{\pi r_0^2}{2Z_0} \left[1 - \left(\frac{f_{CO}}{f}\right)^2\right]^{\frac{1}{2}} \left[1 + \left(\frac{V_{\rho m}^2}{\rho}\right)^2\right] E_{wall,max}^2 \qquad \text{Equation 4.3.1}$$

where P_{TE} is the maximum power expected to be generated (500 MW), r_0 is the radius of the aperture (10.16 cm), Z_0 is the impedance of free space (377 Ω), f_{CO} is the TE_{11} cutoff frequency of the aperture, f is the operating frequency (2.43 GHz), $V_{\rho m}$ is the Bessel function crossing used for the TE_{11}-mode (1.841), and ρ is from the $TE_{\rho m}$.

$$f_{CO} = \frac{c}{2\pi}\left(\frac{V_{\rho m}}{r_o}\right) = 8.652 \text{ MHz} \qquad \text{Equation 4.3.2}$$

$$500 \text{ MW} = \frac{\pi 0.1016^2}{2*(377)} \left[1 - \left(\frac{8.652 \text{ MHz}}{2.43 \text{ GHz}}\right)^2\right]^{\frac{1}{2}} \left[1 + \left(\frac{1.841^2}{1}\right)^2\right] E_{wall,max}^2$$

$$E_{wall,max} = 9.981 \times 10^5 \left[\frac{V}{m}\right] = 9.98 \left[\frac{kV}{cm}\right]$$

It has been shown experimentally that the dielectric strength of air is roughly $30 \left[\frac{kV}{cm}\right]$; thus, we can see that the aperture of the conical horn antenna is more than sufficient to radiate 500 MW.

Chapter 5

Experimental Results

In this chapter the final assembly and experimental results are presented. The initial results did not show good agreement; therefore, some supplementary simulations were conducted to match the experimental results. These comparisons and the conclusions drawn from them are presented.

5.1.1 Final Assembly

The magnetron was attached to the pulser. The electromagnets were installed around the magnetron in the Helmholtz configuration to provide a uniform magnetic field in the interaction space of the magnetron, as shown in Fig. 5.1. The transparent cathode was installed with a precision of 0.001" radially. Furthermore, the cathode strip was oriented such that its leading edge was positioned 5° off of the edge of the vane, as shown in Fig. 5.2. Simulations showed this to be the optimal angle at which maximum power was observed [11]. The beam dump was attached downstream of the magnetron to collect the leakage current and prevent damage to the dielectric window of the conical horn antenna which follows the beam dump. The final aperture of conical horn antenna was optimized for maximum power radiation. Lead bricks surround the magnetron to absorb the X-rays produced by the high-energy electrons bombarding the anode block.

The oil-breakdown switch gap was set to 5.9 mm to provide a load voltage of approximately 350 kV. Two D-dot probes, located before and after the oil-breakdown switch, respectively measured the PFL voltage and the load voltage. Two Rogowski coils were installed upstream and downstream of the anode block to measure the total and leakage currents, respectively. A D-band waveguide detector was positioned opposite the conical horn antenna in the maximum field region to capture the RF signal and measure the frequency.

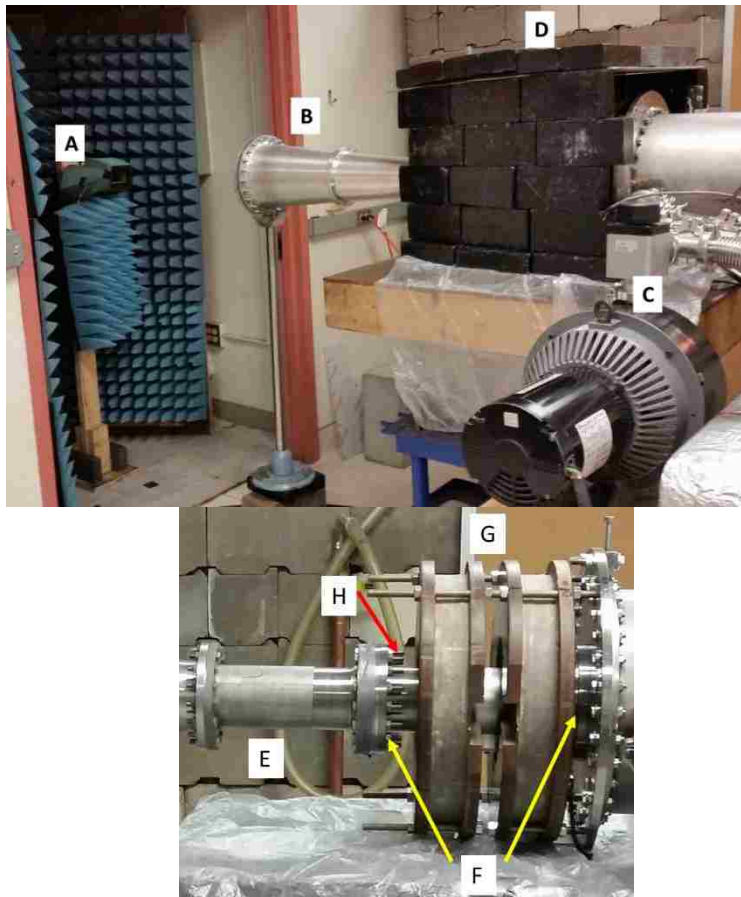**Figure 5.1 (Top) is a photograph of the physical setup where A is the waveguide detector, B is the conical horn antenna, C is the vacuum system, and D is the lead brick shielding over the magnetron. (Bottom) is a photograph of the area shielded by the lead bricks where E is the beam dump, F is the Rogowski coils, G is the Helmholtz coils, and H is the A6 magnetron.**
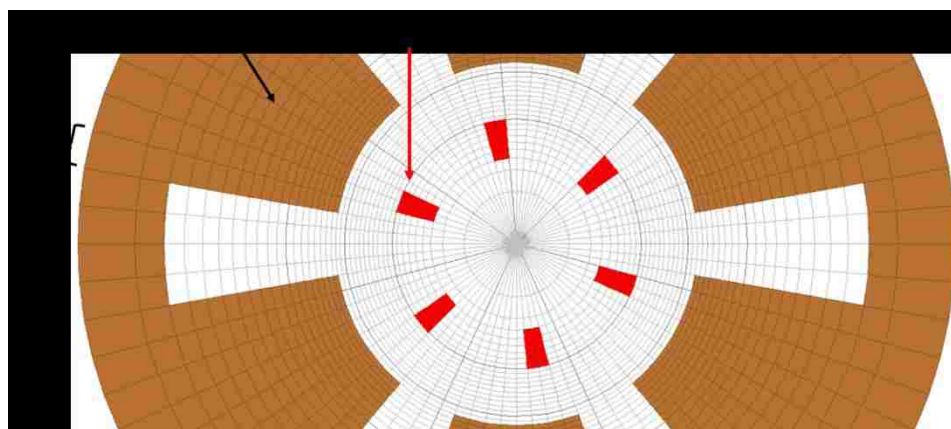

Figure 5.2 The optimal location of the cathode strips.

The vacuum system used consisted of a Tri-scroll roughing pump in conjunction with a turbo pump. The vacuum level achieved was 5.2×10^{-6} Torr. The Marx bank switches were pressurized with SF_6 to 19-23 psi, and charged to 34-36 kV. The operating conditions for the Marx trigger circuit were 54 psi and 54 kV.

A Stanford delay generator was used to send two trigger signals; the first signal discharges the pulsed electromagnetic circuit, to generate the magnetic field, and the second signal is sent after a delay of 24 ms to discharge the Marx bank. This was done to ensure the magnetic field was at maximum during the time of operation of the magnetron.

With the load voltage held fixed at ~350 kV, a magnetic field (B-field) scan in the range of 0.40 T to 0.60 T was conducted. The PFL voltage, load voltage, anode current, leakage current, and RF frequency were recorded for each magnetic field.

Figure 5.3 shows the PFL and load voltage dependence on the applied magnetic field. The data shows that these voltages were fairly constant over the range of magnetic fields. The PFL and load voltages are 700 kV and ~350 kV, respectively. Figure 5.4 shows how the anode and leakage current vary with magnetic field. As expected, the anode current decreased and the leakage current increased with increasing magnetic field. The maximum anode current was measured to be 12.5 kA, and the leakage current was 3 kA. Interestingly, the experimentally measured anode current was rather less than current seen in simulations.

Figure 5.5 is a graphical summary of the microwave power and frequency dependence on magnetic field. The power presented in this curve was determined from the RF amplitude, with the waveguide detector held at a fixed position. The RF frequency was calculated by performing an FFT using a MATLAB script [31]. The power had a tendency to increase as the magnetic field increased, with some fluctuations corresponding to the fluctuations observed in the anode current. Furthermore, a frequency of 2.33 GHz was detected over a wide range of magnetic fields. However, this varied from the 2.43 GHz expected frequency from simulations. A neon grid was used to confirm the RF mode pattern at 2.33 GHz; it is clear that the TE_{11}-mode is dominant, as indicated from the brightness of the neon bulbs in the center of the pattern shown in Fig. 5.6. As a sanity check, a photograph was also taken at a non-optimal magnetic field, which exhibited multiple frequencies, as shown in Fig. 5.7. Clearly the photograph captured does not

show a clean pattern, as in the previous case. The small bright spot in the center is due to the presence of the 2.33 GHZ signal.
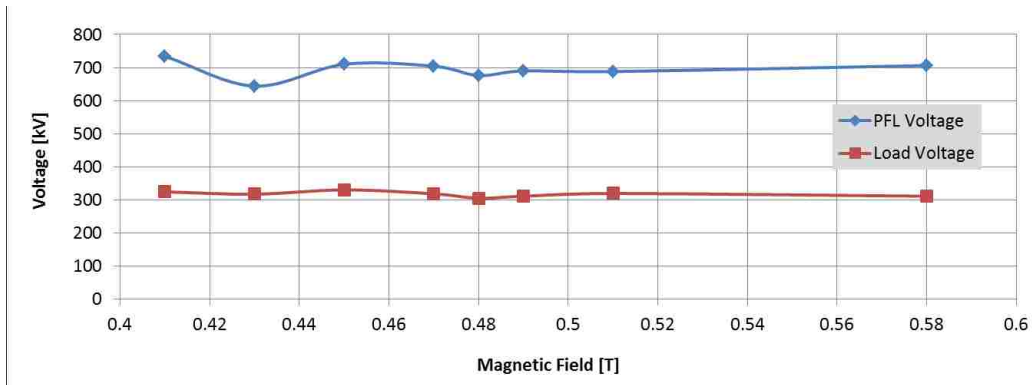
Figure 5.3 The PFL and load voltage dependence on the applied magnetic field.
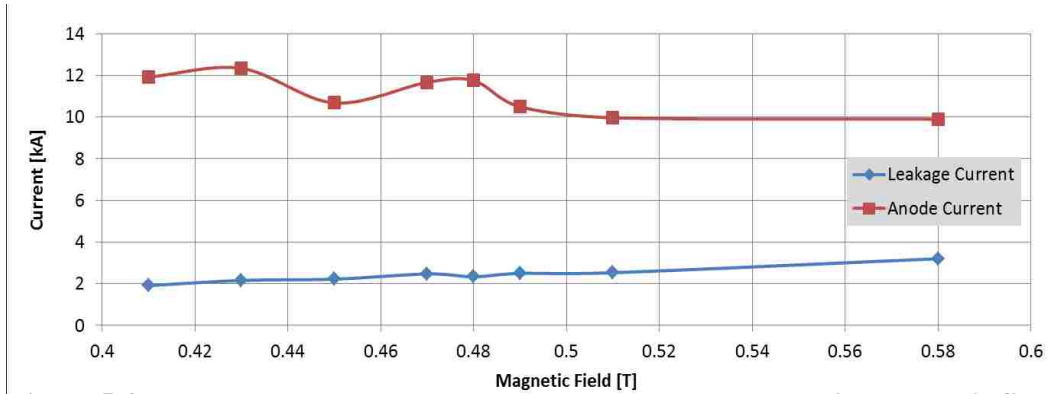
Figure 5.4 The anode and leakage current dependence on the applied magnetic field.
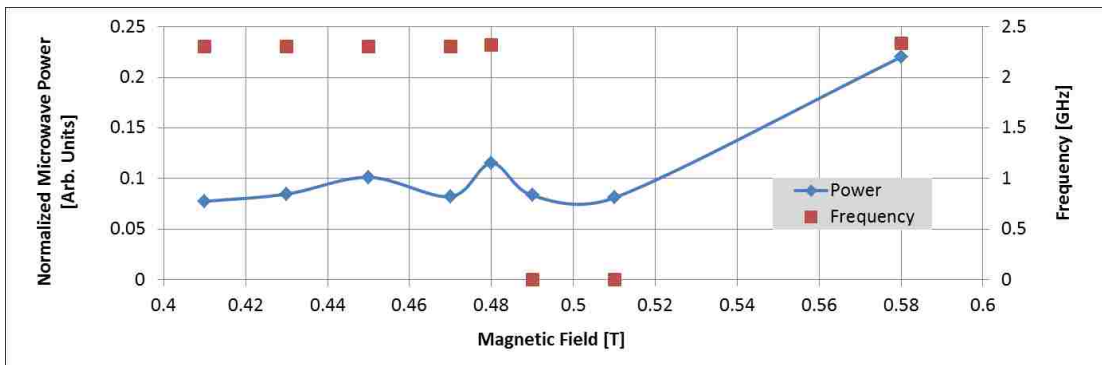
Figure 5.5 The power and frequency dependence on the applied magnetic field.
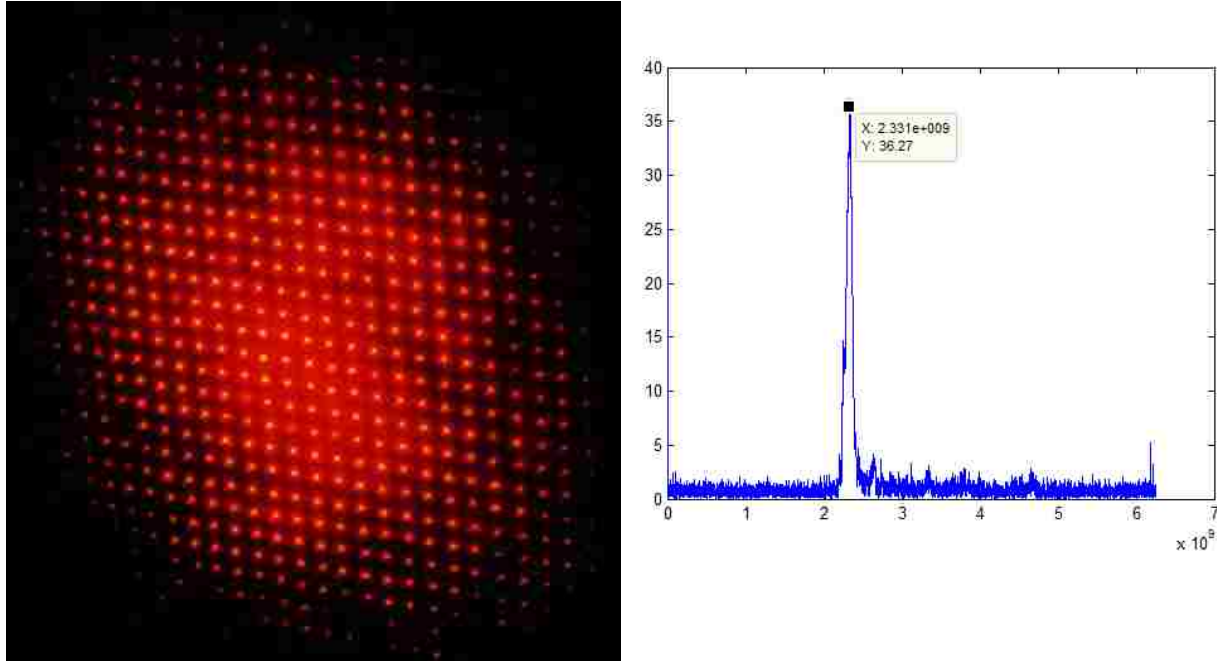
Figure 5.6 Photograph of the neon grid captured with a long exposure digital camera indicating the TE$_{11}$-mode (left), and the FFT of the RF signal for this shot (right).
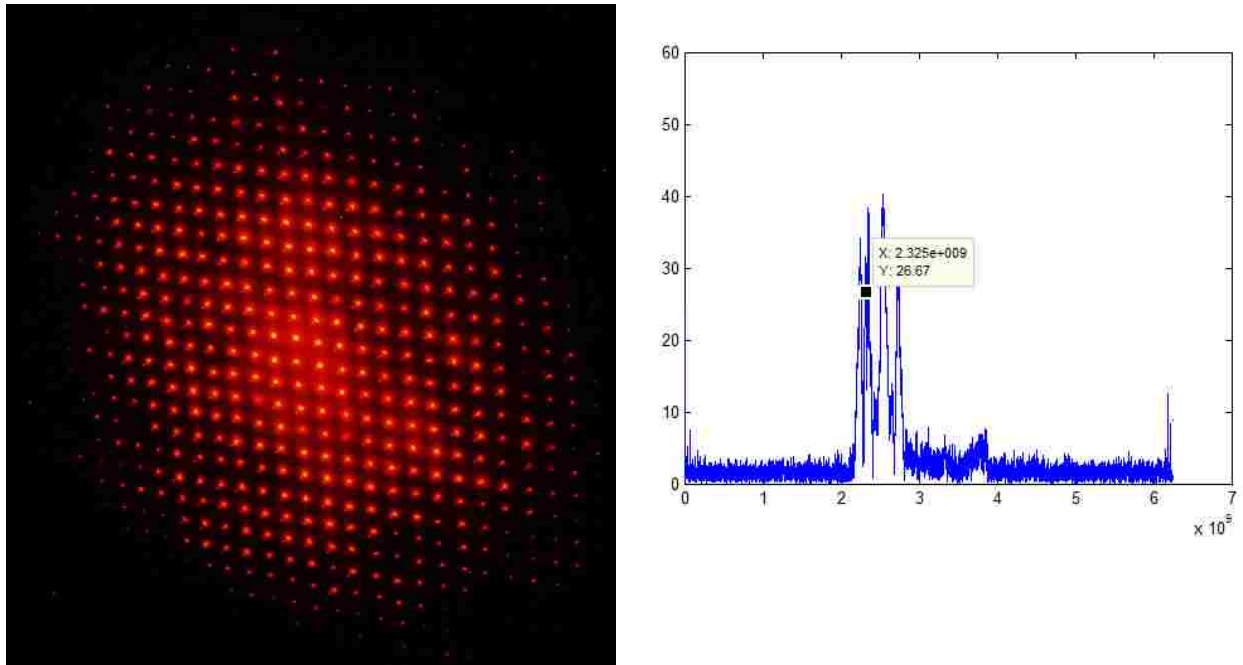
Figure 5.7 Photograph of the neon grid captured with a long exposure digital camera indicating mode competition (left), and the FFT of the RF signal for this shot (right).

Since the experimentally measured frequency corresponding to the TE_{11}-mode contradicted the initial simulation results, supplementary simulations were performed to gain further understanding. The emission region of the cathode in the simulations was set to match the manufactured cathode dimensions. Furthermore, the magnetic field function that dumps the leakage electrons was optimized to match the leakage current measured experimentally. Further investigation is being carried out with the MAGIC code development team to better understand the code anomalies. With these modifications, agreement between simulations and experiments was achieved, and the results are presented below.

Figure 5.8 is a comparison of the normalized experimental and simulation microwave power, showing similar trends. Figure 5.9 displays the anode and leakage current variation. The anode current was much greater in simulations compared to experiments, but the general trend was similar across the B-field range. It is recommended that the current emission model in MAGIC be studied more carefully to gain an understanding of this discrepancy. The leakage current for the two cases was in good agreement.

The experimentally observed frequencies were reproduced in simulations and the summary is presented in Fig. 5.10. Figure 5.11 is a chart comparing the experimental data at 0.58 T and the simulations at 0.56 T, showing very close agreement. The power and frequency waveforms shown indicate that the 2.33 GHz frequency was dominant early on, but that mode competition took over towards the end of the pulse. This was caused by the mode converter effectively loading two of the magnetron cavities. This loading naturally favored the $\frac{4\pi}{3}$ –mode, making it difficult to enforce the π-mode. However, through the use of an upstream anode strap, this issue could be mitigated.

Figure 5.8 The normalized power dependence on the applied magnetic field for simulated and experimental data.
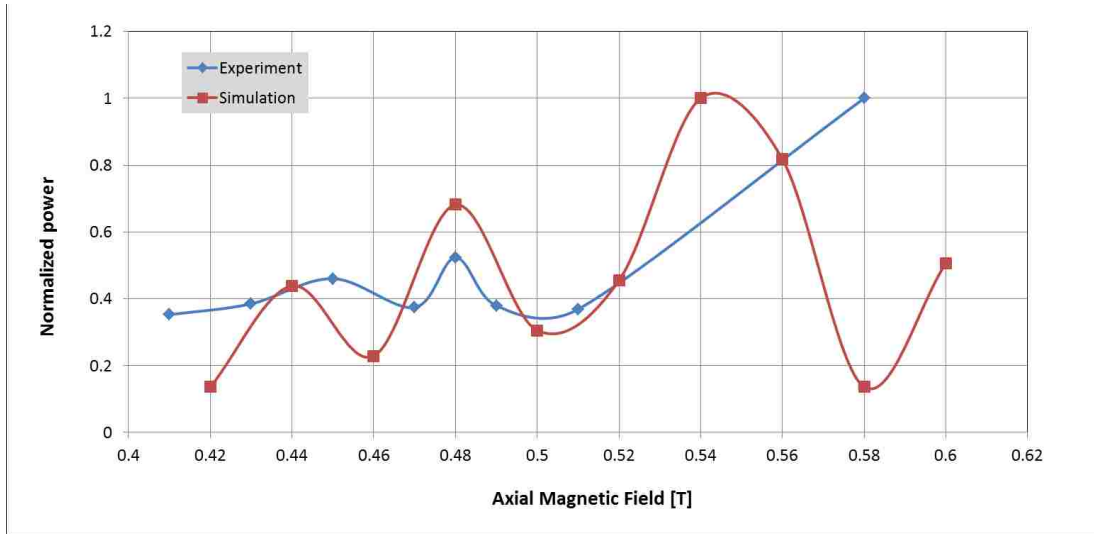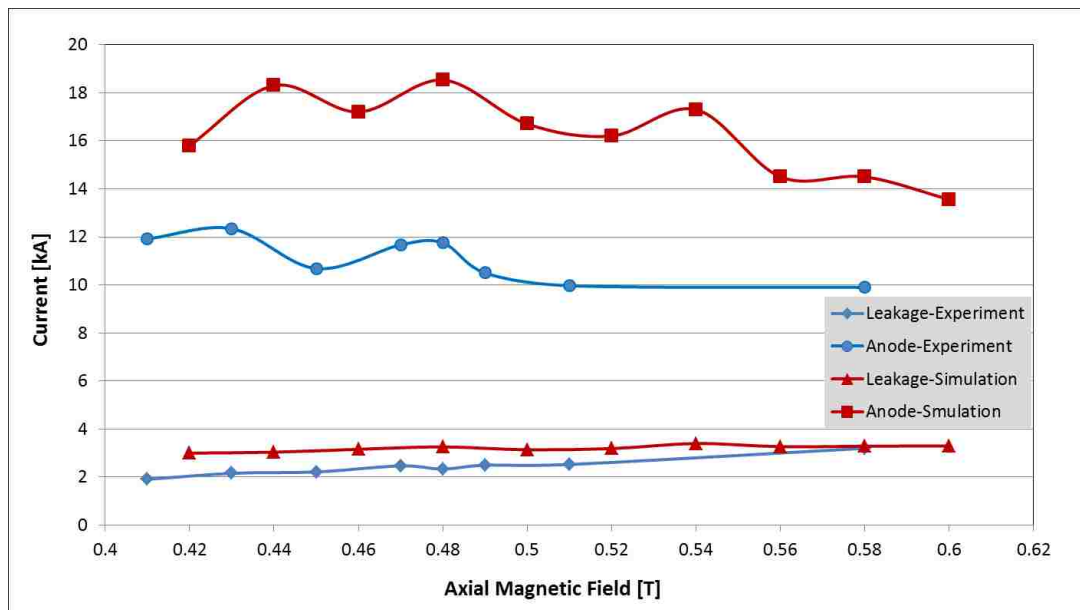

Figure 5.9 Comparison of the anode and leakage current dependence on the applied magnetic field.
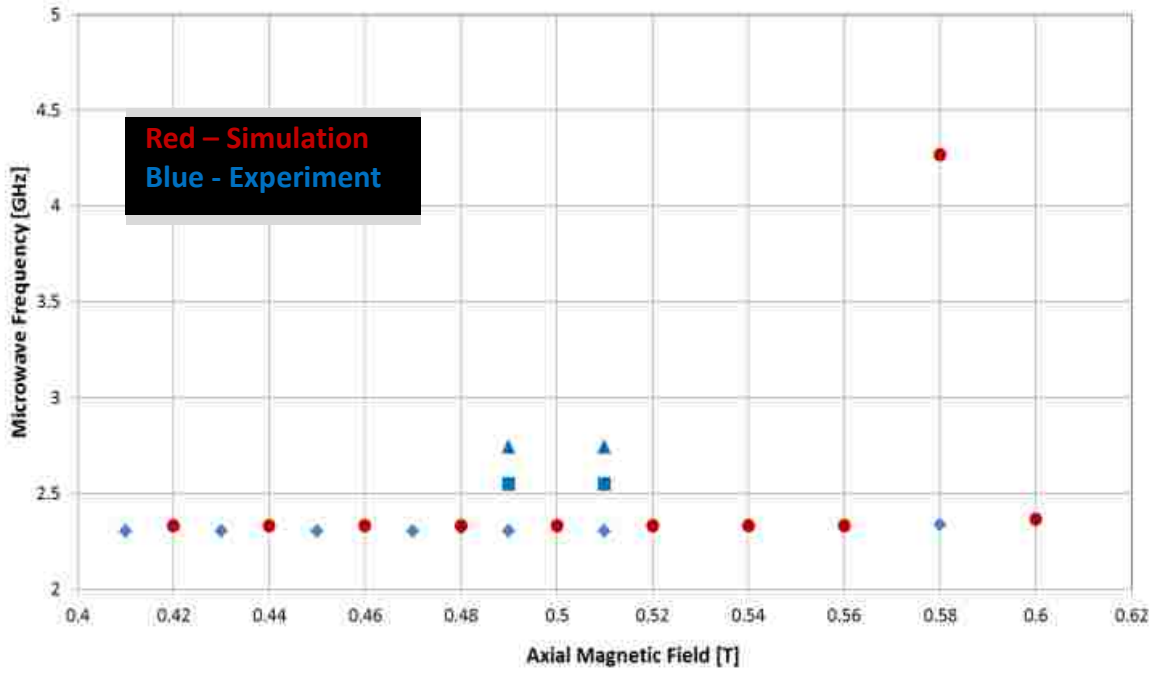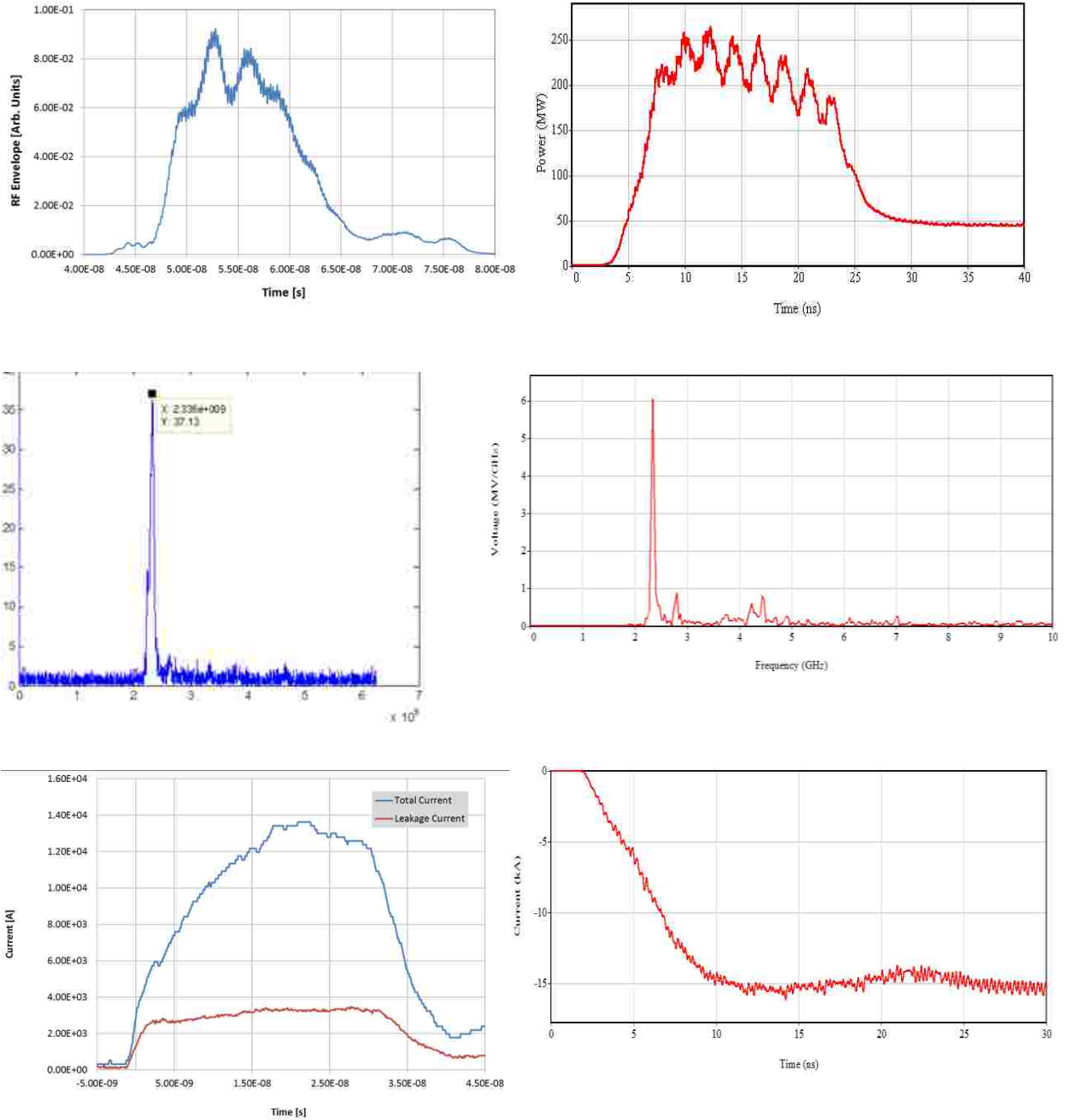
Figure 5.10 Frequency dependence on the applied magnetic field.

Figure 5.11 (Left) experimental results at a magnetic field of 0.58 T; (right) simulation results with updated code showing agreement with experiments.

51

5.1.2 Conclusion

A compact relativistic A6 magnetron with a simple mode converter for axial TE_{11}-mode extraction was proposed. The simple mode converter implements a cavity end cap, with openings which allow the RF to propagate into a circular waveguide. With the magnetron operating in the π-mode, these cavity openings are positioned such that they electrically open the diametrically opposite cavities that exhibit an instantaneous electric field corresponding to the TE_{11}-mode in a waveguide. An extensive parameter sweep was conducted using MAGIC in order to optimize the design of the mode converter. This design was then manufactured and experiments were performed to demonstrate the concept.

Through simulations it was shown that the π-mode could be enforced over a wide range of magnetic fields by reducing the radius of the transparent cathode. For maximum power additional alterations to the cathode were needed, for example it was shown that the length of the cathode strips should start slightly before the anode block, and should not be extend past the downstream end of the interaction space. These simulations showed a very stable π-mode operation with a frequency of 2.43 GHZ over a range the magnetic fields from 0.50 T to 0.60 T. A very clean TE_{11}-mode with a microwave output power of ~480 MW was seen at these parameters. The mode converter and cathode were constructed based on these findings and experimental verification was performed. However, the experimental results showed poor agreement with the initial simulations, in both the frequency seen and the pulse durations of the RF. The frequency of the TE_{11}-mode for the same range of magnetic fields was shown in experiments to be 2.33 GHz, with a pulse width of 15 ns to 20 ns. The pulse shortening was due to the mode competition caused by the mode converter effectively loading the magnetron to favor the $\frac{4\pi}{3}$ –mode, which takes over towards the end of the pulse. Therefore, several modifications to the code were introduced to achieve a better match with the experimental results. This involved building the cathode to match the one which was manufactured. An additional change to the simulation setup was to force the magnetic field function to dump the electrons further away from the interaction space. These changes led to simulations reproducing the experimental results. Due to time constraints and issues with PULSERAD's Marx bank, this design could not be investigated further; however, the concept of the simple mode converter producing a TE_{11}-mode was demonstrated.

5.1.3 Recommendations for Future Work

The experimental results show some discrepancies with the simulations, most notably the increased anode current in simulations. This issue is possibly due to the emission model used by MAGIC, hence further investigation is needed to better understand this discrepancy. Additionally, due to the mode competition observed, the incorporation of an anode strap for enforcing the π-mode should be considered. Using a cathode end cap would eliminate the leakage current, as well as increase the overall efficiency. Another recommendation is to perform an absolute power measurement of the simple mode converter with the HPM calorimeter.

REFERENCES

[1]   J. E. Brittain, "The Magnetron and the Beginnings of the Microwave Age," *Phys. Today*, vol. 38, no. 7, p. 60, 1985.

[2]   J. T. Randall, "The Cavity Magnetron," *Proc. Phys. Soc.*, vol. 58, no. 3, pp. 247–252, 1946.

[3]   H. A. H. Boot and J. T. Randall, "Historical Notes on the Cavity Magnetron," *IEEE Trans. Electron Devices*, vol. 23, no. 7, pp. 51–70, 1976.

[4]   A. Palevsky, "Generation of Intense Microwave Radiation By The Relativistic e-Beam Magnetron Experimental and Numerical Simulation," Massachusetts Institute of Technology, 1980.

[5]   J. Benford, J. Swegle, and E. Schamiloglu, "High Power Microwaves, 3rd Ed. (CRC Press, Boca Raton, FL, 2016).

[6]   E. Schamiloglu, M. I. Fuks, and S. Member, "70 % Efficient Relativistic Magnetron With Axial Extraction of Radiation Through a Horn Antenna," vol. 38, no. 6, pp. 1302–1312, 2010.

[7]   M. Daimon and W. Jiang, "Modified Configuration of Relativistic Magnetron with Diffraction Output for Efficiency Improvement," *Appl. Phys. Lett.*, vol. 91, no. 19, pp. 10–13, 2007.

[8]   M. Daimon, K. Itoh, G. Imada, and W. Jiang, "Experimental Demonstration of Relativistic Magnetron with Modified Output Configuration," *Appl. Phys. Lett.*, vol. 92, no. 19, 2008.

[9]   C. J. Leach, "High Efficiency Axial Diffraction Output Schemes for the A6 Relativistic Magnetron," Ph.D. Dissertation (University of New Mexico, Albuquerque, NM, 2014).

[10]   M. Fuks and E. Schamiloglu, "High Efficiency Relativistic Magnetron With Diffraction Output," pp. 74–80, 2009.

[11]   S. Prasad, "Fast Start of Oscillations in a Short-Pulse Relativistic Magnetron Driven by a Transparent Cathode," Ph.D. Dissertation (University of New Mexico, Albuquerque, NM 2010).

[12]   D.-F. Shi, B.-L. Qian, H.-G. Wang, and W. Li, "A Novel TE $_{11}$ Mode Axial Output Structure for a Compact Relativistic Magnetron," *J. Phys. D. Appl. Phys.*, vol. 49, no. 13, p. 135103, 2016.

[13]   D. F. Shi, B. L. Qian, H. G. Wang, W. Li, and Y. W. Wang, "A Compact Mode Conversion Configuration in Relativistic Magnetron with a TE$_{10}$ Output Mode," *IEEE Trans. Plasma Sci.*, vol. 43, no. 10, pp. 3512–3516, 2015.

[14]   S. Prasad, C. Leach, M. I. Fuks, and E. Schamiloglu, "Compact Relativistic Magnetron with Gaussian Beam Radiation Pattern," in 18th IEEE Int. Conf Pulsed Power (Chicago, June 19- 23, 2011).

[15]   C. Leach, S. Prasad, M. I. Fuks, and E. Schamiloglu, "Compact Relativistic Magnetron with Gaussian Radiation Pattern," *IEEE Trans. Plasma Sci.*, vol. 40, no. 11, pp. 3116–3120, 2012.

[16]   J. McConaha, P. C. Leach, and M. Fuks, "Compact A6 Magnetron with a Neodymium Permanent Magnet," Jeremy McConaha, Sarita, Prasad Chris Leach, Mikhail Fuks, and Edl Schamiloglu," vol. 40, no. 2012, p. 3120.

[17]   C. Leach, S. Prasad, M. Fuks, and E. Schamiloglu, "Compact A6 Magnetron with Permanent Magnet," *2012 IEEE 13th Int. Vac. Electron. Conf. IVEC 2012*, pp. 491–492, 2012.

[18]   V. L. Granatstein, *High-Power Microwave Sources*, (Artech House, Norwood, MA, 1987).

[19]   M. I. Fuks, N. F. Kovalev, A. D. Andreev, and E. Schamiloglu, "Mode Conversion in a Magnetron

with Axial Extraction of Radiation," *IEEE Trans. Plasma Sci.*, vol. 34, no. 3, 2006.

[20] H. Bosman, S. Prasad, and M. Fuks, "Rapid Startup In Magnetrons Using The Transparent Cathode," *Vacuum Electronics Conference 2006 (held jointly with 2006 IEEE International Vacuum Electron Sources)* (Albuquerque, NM, April 25-27, 2006), p. 127-128.

[21] K. S. Yee, "Numerical Solution of Initial Boundary Value Problems Involving Maxwell's Equations in Isotropic Media," *IEEE Trans. Antennas Propag.*, vol. 14, no. 3, pp. 302–307, 1966.

[22] B. Goplen, L. Ludeking, D. Smith, and G. Warren, "User-Configurable MAGIC for Electromagnetic PIC Calculations," *Comput. Phys. Commun.*, vol. 87, nos. 1–2, pp. 54–86, May 1995.

[23] A. J. Woods and L. D. Ludeking, "MAGIC FDTD EM-PIC Solution Improvements and Demonstration on a Plasma Actuator," *2013 International Conference on Electromagnetics in Advanced Applications (ICEAA)* (Torino, Italy, September 9-13, 2013), pp. 78–81.

[24] S. Prasad, C. Leach, K. Prestwich, C. J. Buchenauer, M. Fuks, and E. Schamiloglu, "Experimental Demonstration of the Output Characteristics of the A6 Magnetron on PULSERAD 110a, a Very Short Risetime Accelerator at UNM," *Proc. 2012 IEEE International Vacuum Electronics Conference (Monterey, CA, 24-26 April, 2012), p. 495-496.*

[25] M. Fuks, S. Prasad, and E. Schamiloglu, "Increased Efficiency and Faster Turn-on in Magnetrons using the Transparent Cathode," *Proc. CAVMAG2010* (Bournemouth, UK, April 19-20, 2010), p. 76-81.

[26] J. H. Black, "Solid State Capacitor Discharge Pulsed Power Supply Design for Railguns," M.S. Thesis, Naval Postgraduate School (Monterey, CA, 2007).

[27] T. S. Björn Backlund and E. C. Jürg Waldmeyer, "Gate-Drive Recommendations for Phase Control and Bi-directionally Controlled Thyristors," *ABB Application Note 5SYA 2034-02* (2013).

[28] J. Wang, C. Gao, and J. Yang, "Design, Experiments and Simulation of Voltage Transformers on the Basis of a Differential Input D-dot Sensor," *Sensors (Basel).*, vol. 14, no. 7, pp. 12771–12783, 2014.

[29] I. A. Metwally, "Design of Different Self-integrating and Differentiating Rogowski Coils for Measuring Large-Magnitude Fast Impulse Currents," *IEEE Trans. Instrum. Meas.*, vol. 62, no. 8, pp. 2303–2313, 2013.

[30] L. A. Kojovic and R. Beresh, "Practical Aspects of Rogowski Coil Applications to Relaying," *IEEE PSRC Spec. Rep.*, no. September, pp. 1–72, 2010.

[31] W. Huang and D. L. Macfarlane, "Fast Fourier Transform and MATLAB Implementation" https://www.utdallas.edu/~dlm/3350%20comm%20sys/FFTandMatLab-wanjun%20huang.pdf.

[32] A. G. Shkvarunets, "A Broadband Microwave Calorimeter of Large Cross Section," *Instruments Exp. Tech.*, vol. 39, no. 4, pp. 535–538, 1996.

[33] A. I. Klimov, P. V. Vykhodtsev, A. A. Elchaniniov, O. B. Kovalchuk, I. K. Kurkan, S. D. Polevin, E. M. Totmeninov, and V. V. Rostov, "A Calorimeter for High Power Microwave Pulse Measurement," *Proc. 15th Int. Symp. High Current Electron.*, pp. 422-424, 2008.

[34] D. Meeker, "Finite Element Method Magnetics Version 4.2 User Manual," p. 158, 2015 (http://www.femm.info/Archives/doc/manual42.pdf).